https://doi.org/10.5194/egusphere-2026-4193
Preprint. Discussion started: 23 July 2026

Stratospheric aerosol forcing for CMIP7 – Part 3: comparison with CMIP6 and evaluation using complementary datasets

Man Mei Chim[1], Dominik Stiller[2], Elisa Ziegler[3], Thomas J. Aubry[4,5], Lucas Boissel[6,7,8], Sébastien Guillet[9], Brennan Rodgers[10], Matthew Toohey[10], Christine Pohl[11,12], and Alexei Rozanov[11]

[1]Department of Mathematics and Statistics, University of Exeter, Exeter, United Kingdom
[2]Department of Atmospheric and Climate Science, University of Washington, Seattle, WA, USA
[3]Department of Geosciences, University of Tübingen, Tübingen, Germany
[4]Department of Earth Sciences, University of Oxford, Oxford, United Kingdom
[5]Department of Earth and Environmental Sciences, University of Exeter, Penryn, Cornwall, United Kingdom
[6]Université Paris Cité, Paris, France
[7]Pôle de recherche pour l'organisation et la diffusion de l'information géographique (PRODIG), Paris, France
[8]Laboratoire de Géographie Physique: Environnements Quaternaires et Actuels (LGP), Thiais, France
[9]Climate Change Impacts and Risks in the Anthropocene (C-CIA), Institute for Environmental Sciences, University of Geneva, Geneva, Switzerland
[10]Institute of Space and Atmospheric Studies, University of Saskatchewan, Saskatoon, Canada
[11]Institute of Environmental Physics, University of Bremen, Bremen, Germany
[12]Now at the Department of Physics, Lund University, Lund, Sweden

Correspondence: Man Mei Chim (m.m.chim@exeter.ac.uk), Dominik Stiller (dstiller@uw.edu), and Elisa Ziegler (elisa.ziegler@uni-tuebingen.de)

Abstract. Volcanic stratospheric aerosols represent a key forcing for climate simulations in Phase 7 of the Coupled Model Intercomparison Project (CMIP7). The CMIP7 stratospheric aerosol forcing datasets consist of: i) a volcanic sulfur emission inventory; and ii) stratospheric aerosol optical properties, derived from emissions using a reduced-complexity volcanic aerosol model for 1750–1978, and from satellite observations for 1979–2023. Here, we compare the CMIP7 and CMIP6 stratospheric aerosol forcing datasets over the historical period, and evaluate them against an extensive compilation of observational datasets, including lunar eclipse, stellar extinction, pyrheliometers, lidar, and satellite datasets. CMIP6 and CMIP7 show reasonable agreement (< 20% difference) on peak stratospheric aerosol optical depth (SAOD) for most large-magnitude eruptions including Krakatau (1883), Katmai (1912), Agung (1963), El Chichón (1982), and Pinatubo (1991). For small-to-moderate eruptions, SAOD is likely underestimated in CMIP6 during periods when no such eruptions are included, such as 1940–1960, while CMIP7 includes more pre-satellite small-to-moderate eruptions, as supported by lunar eclipse data. Observational datasets indicate that SAOD perturbations for some moderate-magnitude eruptions, including the 1902, 1921, 1928, 1929, and 1974 eruptions, are captured in CMIP6, but likely underestimated in CMIP7. In addition, independent lidar and stellar extinction measurements show that both CMIP6 and CMIP7 underestimate SAOD over the Northern Hemisphere after the 1982 El Chichón eruption due to observational gaps in satellite instruments. Our findings highlight the potential value of combining CMIP6's use of available observational constraints with CMIP7's extensive emission inventory to refine stratospheric aerosol forcing in future CMIP phases.

https://doi.org/10.5194/egusphere-2026-4193
Preprint. Discussion started: 23 July 2026

1 Introduction

Stratospheric aerosol forcing, arising primarily from explosive volcanic eruptions, is a key input for climate experiments of the Coupled Model Intercomparison Project (CMIP). Explosive volcanic eruptions can inject sulfur dioxide (SO_2) into the stratosphere, where it oxidises to form sulfate aerosols, which can reflect incoming solar radiation and absorb longwave and shortwave radiation, leading to global surface cooling effects (McCormick et al., 1995). General circulation models that contributed historical simulations to Phase 5 of CMIP (CMIP5) used five different stratospheric aerosol optical properties datasets (Xing et al., 2020), though most models relied on two forcing datasets from Ammann et al. (2003) and Sato et al. (1993). To ensure consistent forcing input across models and facilitate direct comparison of model results, a common stratospheric aerosol forcing dataset (Luo, 2018) was used for models participating in CMIP6. CMIP7 introduces major methodological updates, including:

1. The creation of a volcanic SO_2 emission dataset, for the first time for CMIP, using recent ice-core (Sigl et al., 2015; Toohey and Sigl, 2017; Fang et al., 2023), satellite (Carn, 2024), and geological (Global Volcanism Program, 2025) datasets.

2. The derivation of pre-satellite era aerosol optical properties from volcanic emissions using a reduced-complexity aerosol model. In contrast, CMIP6 derived aerosol optical properties from sparse pyrheliometric and stellar extinction measurements (Stothers, 1996) and, for seven eruptions, from volcanic emissions (Gao et al., 2008) using an intermediate-complexity aerosol model (Arfeuille et al., 2014).

3. The attempt to reduce the underrepresentation of small-to-moderate magnitude eruptions (defined as 0.3 to 3 Tg SO_2 emission) in the pre-satellite era by using a geological database (Global Volcanism Program, 2025) and a high-resolution ice-core dataset (Fang et al., 2023).

4. Extended temporal coverage before 1850 backwards up to 1750, which includes several eruptions with the largest SO_2 emission in the historical period, such as the 1815 Mt. Tambora eruption.

Importantly, the CMIP7 datasets are also fully documented by Aubry et al. (2026b, a), who provide initial analyses suggesting that the above methodological differences lead to important differences in the magnitude, spatial distribution, and temporal evolution of volcanic forcing between CMIP6 and CMIP7 with implications for climate simulations. However, they provide no detailed assessment of the CMIP6 and CMIP7 differences, nor any evaluation of the CMIP7 dataset against independent data sources.

As climate modelling centres perform CMIP7 Assessment Fast Track simulations with the updated forcing datasets, understanding how stratospheric aerosol forcing has changed from previous CMIP phases is essential for interpreting differences in simulation results across CMIP phases and assessing model performance. In support of the CMIP Climate Forcing Task Team, the Fresh Eyes on CMIP (FEoC) Modern Forcings project was established to evaluate CMIP7 historical forcing datasets. This study, as part of the FEoC Modern Forcings project initiative, provides a comprehensive evaluation of the CMIP6 and CMIP7

https://doi.org/10.5194/egusphere-2026-4193
Preprint. Discussion started: 23 July 2026

stratospheric aerosol forcing datasets. We compare and validate the stratospheric aerosol forcing datasets against available observations. Specifically, we (1) compare global averages and background aerosol climatologies, (2) analyse selected major eruption cases to evaluate their peak forcing magnitudes and temporal evolution, and (3) evaluate the CMIP7 datasets against observational records, including historical observations from lunar eclipses, pyrheliometric measurements, stellar extinction, and multiple satellite records.

This paper is structured as follows: Section 2 provides an overview of the CMIP6 and CMIP7 stratospheric aerosol forcing datasets (Sects. 2.1 and 2.2) and the observational datasets used for comparison in this study (Sects. 2.3 and 2.4). Section 3.1 presents the evaluation of the stratospheric aerosol optical depths (SAOD) over the historical period, including the comparison of climatologies between CMIP6 and CMIP7, the comparison of selected major eruption cases, and validation against observational records. Section 3.2 presents the comparison of effective radius between CMIP6, CMIP7 and satellite observations. Section 3.3 presents the comparison of volume and number density variables in CMIP6 and CMIP7. Section 4 discusses the key differences between the CMIP6 and CMIP7 stratospheric aerosol forcing datasets, their potential implications for climate simulations, and suggestions on the directions for future forcing dataset development.

2 Data description

2.1 CMIP6 stratospheric aerosol forcing

Stratospheric aerosol forcing datasets in CMIP6 and CMIP7 comprise seven variables describing aerosol optical properties: aerosol extinction, asymmetry factor, single scattering albedo, surface area density, volume density, number density, and effective radius. Table 1 shows the summary of the comparison between CMIP6 and CMIP7 stratospheric aerosol forcing datasets used for the historical, pre-industrial control, and scenario forcings. We provide a brief summary of the CMIP6 dataset (version 3.0) here and refer the reader to the CMIP6 documentation (Luo, 2018; Jörimann et al., 2025; Thomason et al., 2018) and the extensive overview in Part 1 of this paper series (Aubry et al., 2026b) for more details.

From 1979, CMIP6 used observed aerosol optical properties derived from the Global Space-based Stratospheric Aerosol Climatology version 1.0 (GloSSAC, Thomason et al., 2018). For 1850–1978, before the satellite era, the CMIP6 forcing is based on a combination of datasets:

1. For the seven large eruptions, aerosol optical properties from an intermediate-complexity aerosol model (AER2D, Arfeuille et al., 2014) were produced using the ice-core-based volcanic sulfur emission inventory (Gao et al., 2008). For some eruptions, the injection mass, latitude, and height were modified to enhance the agreement between simulations and available pyrheliometric measurements (Stothers, 1996).

2. For any period not covered by (1), pyrheliometer, stellar extinction, and lunar eclipse data (Stothers, 1996, 2001, 2007) were used to derive aerosol optical properties of “minor” eruptions. For the majority of months with pyrheliometer data available, measurements were available from a single station or location, from which hemispheric-scale aerosol optical properties were derived.

https://doi.org/10.5194/egusphere-2026-4193
Preprint. Discussion started: 23 July 2026

3. For any period not covered by (1) or (2), a climatology derived from the volcanically quiescent 1999–2005 period was imposed for non-volcanic background stratospheric aerosols, with an increasing trend between 1850 and 1978 to account for increasing anthropogenic tropospheric aerosol emissions.

The REMAPv1 algorithm (Jörimann et al., 2025) was used to obtain aerosol optical properties (e.g., extinction coefficient, single-scattering albedo, asymmetry factor) at any wavelength from the source datasets described above. The pre-industrial stratospheric aerosol forcing (Eyring et al., 2016), also imposed in scenario simulations (O'Neill et al., 2016), was taken as the average of the historical period, i.e., the 1850–2014 average. A major strength of the CMIP6 dataset is that it maximises the use of available indirect aerosol optical property measurements to constrain the pre-satellite era dataset. Although these measurements are sparse temporally and spatially, and highly uncertain, they represent some of the only available constraints on pre-satellite stratospheric aerosol optical properties. However, the CMIP6 dataset is characterised by heterogeneous methodologies, and strongly biased in terms of representation of small-to-moderate magnitude eruptions (Chim et al., 2023). Indeed, for 1850–1978, approximately 78 years (60%) have no stratospheric aerosol optical properties perturbation, with the longest unperturbed period in CMIP6 lasting 28 years (Aubry et al., 2026b). This is at odds with the satellite record, which suggests that small-to-moderate magnitude eruptions injecting sulfur into the stratosphere typically occur multiple times per year (e.g., Carn et al., 2016; Schmidt et al., 2018).

2.2 CMIP7 stratospheric aerosol forcing

Here, we briefly summarise the key methodological features of the CMIP7 dataset (version 2.2.1), but refer to Aubry et al. (2026b, a) for a full documentation. Similarly to CMIP6, CMIP7 uses GloSSAC (version 2.22, Kovilakam et al., 2020) for 1979–2023. For the pre-satellite era (1750–1978), CMIP7 derives volcanic perturbations to stratospheric aerosol optical properties from the CMIP7 volcanic SO_2 emission inventory (Aubry et al., 2026a) using the reduced-complexity volcanic aerosol model EVA_H v2 (Aubry et al., 2026b). EVA_H v2 is calibrated against satellite-era emissions and optical properties. The CMIP7 methodology is consistent with the Paleoclimate Model Intercomparison Project (PMIP, Jungclaus et al., 2017) and Volcanic Forcings Model Intercomparison Project (VolMIP, Zanchettin et al., 2016), which also generate volcanic forcing using the EVA_H reduced-complexity model based on volcanic SO_2 emissions.

A stratospheric aerosol background is derived from the volcanically quiescent 1998–2001 period, plus a linear trend between 1850–1978. Stratospheric aerosol optical properties in the pre-satellite era are then the combination of volcanic perturbation and this background. For the pre-satellite era, the CMIP7 volcanic SO_2 emission inventory primarily relies on bipolar ice-core arrays (Sigl et al., 2015; Toohey and Sigl, 2017), complemented by a single, high-resolution Greenland ice-core (Fang et al., 2023) and Volcanic Explosivity Index (VEI) 4 and 5 eruptions from the Global Volcanism Program (Global Volcanism Program, 2025) not detected in ice-core datasets. The inclusion of the latter two datasets enables minimisation of biases associated with under-recording of small-to-moderate magnitude eruptions in the pre-satellite era, an important strength of the CMIP7 dataset which might result in cooler CMIP7 simulations for the early historical period (Aubry et al., 2026b). However, one weakness compared to CMIP6 is that existing indirect constraints on aerosol optical properties in the pre-satellite era (e.g., pyrheliometer

Table 1. Summary of CMIP6 and CMIP7 stratospheric aerosol forcing datasets for historical, pre-industrial control, and scenario forcings.

Stratospheric aerosol optical properties	**CMIP6**	**CMIP7**
Pre-industrial	Average of the historical (1850–2014) period (global-mean SAOD at 550 nm: 0.0107) (Eyring et al., 2016).	Average of the historical (1850–2021) period (global-mean SAOD at 550 nm: 0.0135) (Aubry et al., 2026b; Dunne et al., 2024).
Pre-satellite period (1850–1978 for CMIP6, 1750–1978 for CMIP7)	Derived from lunar eclipses, pyrheliometric, and stellar extinction measurements (Stothers, 1996, 2001), except for seven major eruptions, which are emission-derived using the ice-core based emissions from Gao et al. (2008) and the AER2D intermediate-complexity aerosol model.	Emission-derived using the EVA_H v2 reduced-complexity volcanic aerosol model (Aubry et al., 2020, 2026b) and the CMIP7 volcanic SO_2 emission inventory (Aubry et al., 2026a).
Satellite period (1979–2014 for CMIP6, 1979–2023 for CMIP7)	Satellite-derived using GloSSAC v1.0 (Thomason et al., 2018).	Satellite-derived using GloSSAC v2.22 (Kovilakam et al., 2020).
Scenario forcing	Same as pre-industrial, with a 10-year linear ramp from the end of historical period (Dec 2014) (O'Neill et al., 2016).	Same as pre-industrial, with a 9-year ramp from the end of historical period (Dec 2021) (Aubry et al., 2026b; Dunne et al., 2024).

measurements) are not used. This is a key motivation for this follow-up evaluation paper. Similar to the CMIP6 protocol, pre-industrial aerosol optical properties are derived from their historical (1850–2021 for CMIP7) averages, and scenario optical properties are equal to pre-industrial ones with a linear ramp (9-year in CMIP7) from the end of the historical period for harmonisation.

2.3 Datasets used for evaluation

In our analysis, we compare CMIP7 stratospheric aerosol properties against the most widely used volcanic forcing input datasets in CMIP5 (Sato et al., 1993; Ammann et al., 2003; see Table 2 in Xing et al., 2020) and CMIP6 (Luo, 2018). We also evaluate the CMIP7 stratospheric aerosol properties using independent observational datasets, including stratospheric aerosol optical properties derived from lunar eclipses, pyrheliometric measurements, stellar extinction, ground-based lidar measurements, and satellite retrievals. These include data used in CMIP6 as well as new data. Figure 1 summarises the datasets used for the comparison in this study.

https://doi.org/10.5194/egusphere-2026-4193
Preprint. Discussion started: 23 July 2026

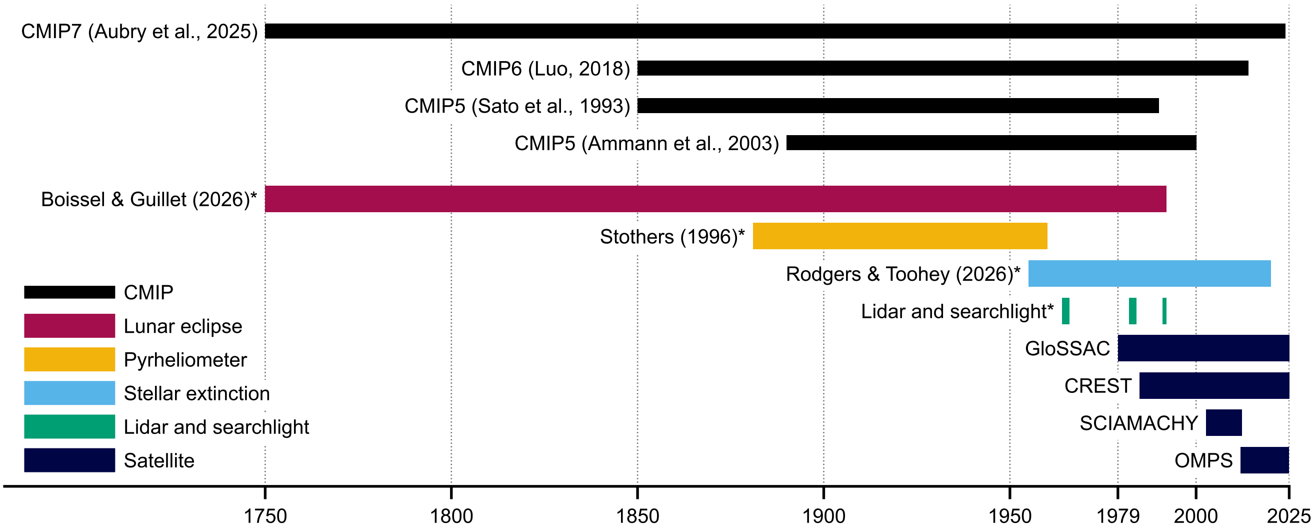

Figure 1. Availability of datasets used for comparison. The non-CMIP7 datasets were chosen since they are largely independent from the CMIP7 dataset. Asterisks (*) indicate that a dataset is not spatially resolved; rather, it is globally integrated (for lunar eclipse) or pointwise (for pyrheliometer, stellar extinction, lidar, and searchlight; possibly at multiple sites).

2.3.1 Lunar eclipse

Lunar eclipse observations can provide semi-quantitative constraints on stratospheric aerosol loading. During a total lunar eclipse, the only solar radiation reaching the Moon's surface has been refracted tangentially through Earth's atmosphere, where it is scattered and absorbed by aerosols and gases before being projected onto the lunar disk. Under atmospheric conditions with low stratospheric aerosols, the Moon appears copper-red to orange in colour. Following explosive volcanic eruptions that inject sulfur into the stratosphere, scattering and absorption are particularly strong, producing anomalously dark eclipses ranging from dim red to nearly invisible. Upper-tropospheric aerosols may affect the brightness of the Moon, but such an effect is limited (Keen, 1983; Hofmann et al., 2003; Matsushima et al., 1966). The brightness and colour of lunar eclipses are systematically classified using the Danjon luminosity scale (Danjon, 1921), with values of $L \in \{0,1,2,3,4\}$. The lowest value $L = 0$ corresponds to very dark eclipses with high stratospheric aerosol loading where the Moon is barely visible to the naked eye, while $L = 4$ denotes bright copper-red eclipses with minimal aerosol loading. Lunar eclipses integrate aerosol loading globally, but may be weighted toward one hemisphere, depending on the eclipse path (Keen, 1983).

Several studies have reconstructed the global-mean SAOD from lunar eclipse observations. Keen (1983) established a systematic conversion of observed eclipse brightness into SAOD estimates based on optical theory for 1960–1982, with later extensions spanning the nineteenth through early twenty-first centuries (Hofmann et al., 2003). Stothers (2004, 2005, 2007) compiled historical descriptions of lunar eclipse observations between 1671 and 1881, establishing a mapping from Danjon's L-values to SAOD estimates ranging from 0 to 0.1 based on Keen (1983). Guillet et al. (2023) refined Stothers' empirical rela-

https://doi.org/10.5194/egusphere-2026-4193
Preprint. Discussion started: 23 July 2026

tionship by assigning SAOD intervals rather than single values to each Danjon class. They then reconstructed the global-mean SAOD from historical texts of lunar eclipse observations for the period 1100–1300.

Most recently, Boissel and Guillet (2026) extended the SAOD reconstruction to cover 1750–2022 by compiling historical sources including astronomical journals, newspaper accounts, and observation reports. Adopting the methodology of Guillet et al. (2023), this reconstruction provides the global-mean SAOD time series at 550 nm for 190 events (>1500 observations) with uncertainty bounds for each luminosity class. For the darkest classification ($L = 0$), the lower SAOD bound is revised from 0.1 to 0.08 since observations of 1963 Agung and 1982 El Chichón eruptions, both assigned with $L = 0$, do not reach an SAOD value of 0.1. The $L = 0$ values represent only a lower bound rather than a range, as the Moon becomes effectively invisible beyond this threshold. They also introduce intermediate Danjon values of $L \in \{0.5, 1.5, 2.5, 3.5\}$ to account for ambiguous visual descriptions.

The eclipse-derived SAOD reconstruction represents broad estimates of stratospheric aerosol loading consistent with the observed eclipse brightness. There is substantial uncertainty for $L \geq 1$ since the classification is subjective and depends on observer experience and local weather conditions. For instance, if a lunar eclipse occurs when the Moon is low on the horizon (e.g., near sunrise or sunset), twilight conditions can make the Moon appear darker than usual. Only when $L = 0$ are lunar eclipse observations a reliable indicator of major volcanic eruptions. Nonetheless, lunar eclipses provide valuable constraints for reconstructing historical stratospheric aerosol forcing particularly for the pre-instrumental period when no other measurements are available, and serve as a complementary source of information for the satellite period.

2.3.2 Pyrheliometric measurements

A pyrheliometer is a ground-based instrument that measures direct solar irradiance across the broad solar spectrum (wavelengths of $\sim$0.3–2 μm), which can be used to derive atmospheric optical depth (Stothers, 1996). To isolate the optical depth component attributed to volcanic aerosols, a reference baseline method is used, whereby cloud-free solar observations at equivalent air mass and time of year are compared between volcanically perturbed and unperturbed periods at the same station (Stothers, 1996). A limitation of this approach is that the computed aerosol optical depths may exhibit negative values during periods of low volcanic activity, and the baseline may be affected by other non-volcanic aerosol sources and atmospheric trace gases.

We use the pyrheliometric optical depth dataset from Stothers (1996), which reports the hemispheric monthly-mean pyrheliometric measurements from a total of 23 stations between 1881 and 1960. The majority of the stations were located between 30°N–60°N, with three stations operated at 23°S–35°S from 1926–1936. Stothers (1996) identified and reported the hemispheric-mean pyrheliometric optical depth for 10 major volcanic eruptions, including Krakatau (1883), an unidentified event (1890), Soufrière St. Vincent/Pelée (1902), Santa María (1902), Ksudach (1907), Katmai (1912), Puyehue (1921), Paluweh (1928), Komagatake (1929), and Quizapu (1932). The pyrheliometric optical depth is assumed to be zero for months without volcanic perturbations. The number of pyrheliometer measurements for the identified eruptions ranges between 1 station (i.e., Krakatau, 1890 event, Paluweh, Komagatake, Quizapu) and 14 stations (i.e., Katmai) (Fig. S1). The pyrheliometric optical depth for each eruption is obtained by taking the mean of the measurements from the available station(s). The optical

https://doi.org/10.5194/egusphere-2026-4193
Preprint. Discussion started: 23 July 2026

depths for four eruptions, including Krakatau, the 1890 eruption, Santa María, and Katmai, are assumed to decay exponentially with time with an e-folding time ranging between 0.8 and 1 year. To obtain SAOD at 550 nm, the mean pyrheliometric optical depth is then multiplied by a factor of 1.6 as described in Stothers (1996). In the CMIP6 dataset, the SAOD at 550 nm is derived from scaling Stothers (1996) pyrheliometric optical depth by an unspecified aerosol size dependent conversion factor between 1.2 and 1.5 (Luo, 2018). The pyrheliometer stations used in CMIP6 are listed in Figure S1.

2.3.3 Stellar extinction

Enhancements to the stratospheric aerosol layer from major volcanic eruptions can be quantified by measurements of the resulting apparent dimming of starlight, known as stellar extinction, from standard reference stars known to be not intrinsically variable in brightness (Hardie, 1962; Stothers, 2001). Stellar extinction coefficients are derived by taking repeated measurements of the apparent brightness of standard stars at different zenith angles as the star rises or sets throughout the course of the night. By combining the Beer–Lambert law with Pogson's equation from astronomy, a linear relationship between apparent magnitude (i.e., the logarithm of apparent brightness) and the relative air mass (i.e., the ratio of air column density at the observed zenith angle to the air column density at zenith) can be obtained. The stellar extinction coefficient a for a given date and location corresponds to the best-fitting slope of this relationship. To convert this coefficient to optical depth τ, the conversion $\tau = 0.921a$ is used, which arises as a natural consequence from combining exponential attenuation with the logarithmic definition of apparent magnitude (Hardie, 1962; Stothers, 2001).

These coefficients may provide useful information for atmospheric and climate scientists (Stock, 1969). To estimate the SAOD at each measurement site, it is commonly assumed that the other components of the total optical depth, including the tropospheric aerosol optical depth, Rayleigh scattering, and the influence of ozone and other gas species are constant from year to year. Under this assumption, an optical depth anomaly produced by subtracting a monthly-varying baseline for a reference period undisturbed by volcanic activity from each time series provides an estimate of SAOD (Stothers, 1996, 2001). Since the quality of astronomical observations is related to the transparency of the sky, it is desirable for astronomical observatories to be at high elevation or locations with generally low tropospheric aerosol content. This assumption that the other components of total optical depth are constant from year to year is thus more appropriate for astronomical observatories than it would be in general due to astronomical observatories typically being located to minimise the effect of tropospheric contamination (García-Gil et al., 2010). Good agreement has been found when comparing annual means of SAOD derived from stellar extinction to those derived from satellite measurements for periods where both are available (Fig. S2), with Rodgers (2022) obtaining a mean percent difference of approximately 14.5% and Stothers (2009) finding differences of similar magnitude.

Stothers (2001) compiled stellar extinction data from available literature, estimating SAOD at nine locations in the subtropics of both the Northern and Southern hemispheres, over the period 1961–1978. Building on this effort, Rodgers (2022) compiled and digitised the original data sources used by Stothers (2001), added data from additional sites, and extended coverage to 2020. They also updated the SAOD estimation method by introducing median-based thresholding to the determination of the reference period baseline which improves the accuracy of the reference period by excluding outliers in the raw data. They also estimated uncertainties in the derived SAOD values quantified as the 1-σ standard error of the mean based on the number and

https://doi.org/10.5194/egusphere-2026-4193
Preprint. Discussion started: 23 July 2026

variability of daily measurements. In this work, we use monthly-mean SAOD at 550 nm and uncertainties reported by Rodgers and Toohey (2026), derived from stellar extinction datasets collected between 1955 and 2020 from twelve measurement sites (six Northern Hemisphere (NH) sites at 28°N–35°N and six Southern Hemisphere (SH) sites at 26°S–34°S, see Table 2.2 in Rodgers, 2022).

2.3.4 Lidar and searchlight measurements

Ground-based lidar and searchlight measurements provide valuable constraints on stratospheric aerosol optical properties, both for eruptions in the pre-satellite era and as validation for satellite retrievals. Such measurements have routinely been collected for decades (e.g., Deluisi et al., 1983; Barnes and Hofmann, 1997), and recent data rescue efforts by the APARC (Atmospheric Processes And their Role in Climate) project have recovered and recalibrated additional lidar and searchlight measurements (Antuña-Marrero et al., 2020b, 2021, 2024). We use these observations to evaluate SAOD following the 1963 Mt. Agung, 1982 El Chichón, and 1991 Mt. Pinatubo eruptions in Section 3.1.5. For the 1963 Agung eruption, we use the searchlight-derived SAOD at 550 nm at White Sands (33°N), and aerosol extinction at 532 nm at Lexington (42°N) and Fairbanks (65°N) with two-way aerosol transmittance correction for January to May 1964 and October 1964 to August 1965 (Antuña-Marrero et al., 2020a, 2023). For the 1982 El Chichón and 1991 Mt. Pinatubo eruptions, we use lidar data at 694 nm from Mauna Loa (20°N; assumed extinction-to-backscatter ratio of 50 sr; John E. Barnes, pers. comm.). For the 1991 Mt. Pinatubo eruption, we also use lidar data at 353 nm from Table Mountain, California (34°N; assumed extinction-to-backscatter ratio of 50 sr; Thierry Leblanc, pers. comm.) and at 355/532 nm from the Observatoire de Haute-Provence (44°N; assumed extinction-to-backscatter ratio of 40–50 sr; Sergey M. Khaykin, pers. comm.), and shipborne lidar data at 532 nm from two Soviet vessels between 20°N to 40°N (assumed extinction-to-backscatter ratio of 25 sr), which provides transects of the Pinatubo cloud over the Atlantic Ocean from July to September 1991, and from January to February 1992 (Antuña-Marrero et al., 2020c). Daily lidar data are binned to monthly resolution; the number of measurements per bin is variable and may be as low as one. All lidar data are converted to 550 nm for comparison with CMIP6 and CMIP7 datasets (see Sect. 2.4).

Uncertainties in lidar-derived extinction arise from several sources. The dominant uncertainty is the assumed extinction-to-backscatter ratio, which can vary by a factor of three between the background and perturbed conditions and with wavelength (e.g., Jäger and Deshler, 2002). Some authors assume a constant value in time and altitude (e.g., Avdyushin et al., 1993; Antuña-Marrero et al., 2020c) while others use time-varying values, e.g., derived from particle counter measurements of the 1991 Mt. Pinatubo aerosol cloud, even for other eruptions (Antuña-Marrero et al., 2021). Further uncertainties arise from the backscatter retrieval itself (Russell et al., 1979) and from the conversion to a target wavelength.

2.3.5 Satellite products

For the satellite era (after 1979), the CMIP7 stratospheric aerosol forcing dataset is based on extinctions from GloSSAC (Kovilakam et al., 2020). The 525-nm extinction is copied directly from GloSSAC. All other optical properties, such as the extinction at other wavelengths and the effective radius, are derived from the 525-to-1020-nm extinction ratio based on Mie scattering theory with simplifying assumption on the aerosol size distribution (Aubry et al., 2026b). We compare these derived values

https://doi.org/10.5194/egusphere-2026-4193
Preprint. Discussion started: 23 July 2026

in CMIP7 against other satellite datasets, which use different measurement techniques and retrieval assumptions. GloSSAC is based on SAGE II/III solar occultation measurements, supplemented mainly by OSIRIS limb-scattering and CALIOP lidar data. In contrast, the comparison datasets are mostly based on limb scattering (e.g., OMPS-LP and SCIAMACHY). Solar occultation measurements are taken at local sunrise and sunset and are based on direct (attenuated but not scattered) radiation from the sun, leading to sparse spatial and temporal sampling. Limb-scattering improves sampling coverage, but retrieving extinction involves radiative transfer modelling with assumptions on particle size and aerosol composition.

OMPS-LP ("Ozone Mapping and Profiler Suite Limb Profiler") limb-scattering data are available after 2012. We use the retrievals of stratospheric aerosol extinction from Rozanov et al. (2024). We apply the CMIP7 troposphere mask to OMPS-LP and exclude data below 12 km since the retrieval quality degrades due to loss of retrieval sensitivity (Rozanov et al., 2024). Other retrievals for OMPS-LP exist (Zawada et al., 2018; Taha et al., 2021) but were not used here. The retrievals differ most after major volcanic eruptions (Kovilakam et al., 2025; Bourassa et al., 2023), but agree reasonably for weaker eruptions.

SCIAMACHY ("Scanning Imaging Absorption Spectrometer for Atmospheric Chartography") limb-scattering measurements are available for 2002–2012. We use the retrievals of particle size distribution parameters from Pohl et al. (2024), from which they derive the extinction and effective radius, validated against balloon-borne measurements and independent satellite retrievals. In a comparison with nudged atmosphere–aerosol simulations, the retrieval was found to provide useful extinction and aerosol size information (Pohl et al., 2026).

CREST ("Climate Data Record of Stratospheric Aerosols") version 2.0 is a merged record of stratospheric aerosol extinction from multiple satellite instruments, transformed to 750 nm (Sofieva et al., 2024b). Beyond some of the source datasets used in GloSSAC (SAGE II, SAGE III, OSIRIS), CREST additionally includes OMPS-LP, GOMOS, and SCIAMACHY data, and the data processing code is independent from GloSSAC. The SCIAMACHY extinction in CREST is retrieved directly from limb-scattering radiances, rather than via the particle size distribution as in the Pohl et al. (2024) retrieval described above. Gaps are filled using a 3-month running mean and Delaunay triangulation (Sofieva et al., 2024b).

2.4 Data pre-processing

To compare CMIP7 and other datasets, the extinction needs to be interpolated to a common wavelength. To convert the CMIP7 extinction to another wavelength, we linearly interpolate the provided extinction spectrum. To convert satellite and lidar data from an original wavelength λ_0 to 550 nm, we use the Ångström formula (Ångström, 1929):

$$\beta_{550\ \mathrm{nm}} = \beta_{\lambda_0}\left(\frac{550\ \mathrm{nm}}{\lambda_0}\right)^{-\alpha}, \qquad (1)$$

where β is the extinction coefficient at a given wavelength and α is the Ångström exponent. This conversion may be biased low (by around 10%) since the aerosol extinction spectrum does not exactly follow the Ångström formula. Corrections exist but not for conversion to 550 nm (Damadeo et al., 2024). We use a time-varying zonal-mean α derived from the 525-nm and 1020-nm extinction of CMIP7. During unperturbed periods, α is around 2.0, but it decreases to below 0.5 after the 1991 Mt. Pinatubo eruption due to larger aerosol sizes. For lidar data from Lexington and Fairbanks reported by Antuña-Marrero et al. (2021), we derive the wavelength exponent using the 532 nm and 694 nm aerosol backscatter and extinction.

https://doi.org/10.5194/egusphere-2026-4193
Preprint. Discussion started: 23 July 2026

Since the CMIP7 dataset is for stratospheric aerosols only, tropospheric values are masked. The climatological tropopause as a function of month and latitude is based on the MERRA reanalysis (Aubry et al., 2026b). For vertically integrated values (e.g., SAOD, or vertical-mean effective radius), we apply the CMIP7 tropospheric mask to comparison datasets.

3 Results

3.1 Stratospheric aerosol optical depth over the historical period

The stratospheric aerosol optical depth (SAOD) is the vertically integrated aerosol extinction from the tropopause upwards. It is the primary optical property required by the radiative transfer code in climate models to simulate the radiative forcing and thus climate effects of volcanic eruptions.

3.1.1 Overview and comparison with other datasets

https://doi.org/10.5194/egusphere-2026-4193
Preprint. Discussion started: 23 July 2026

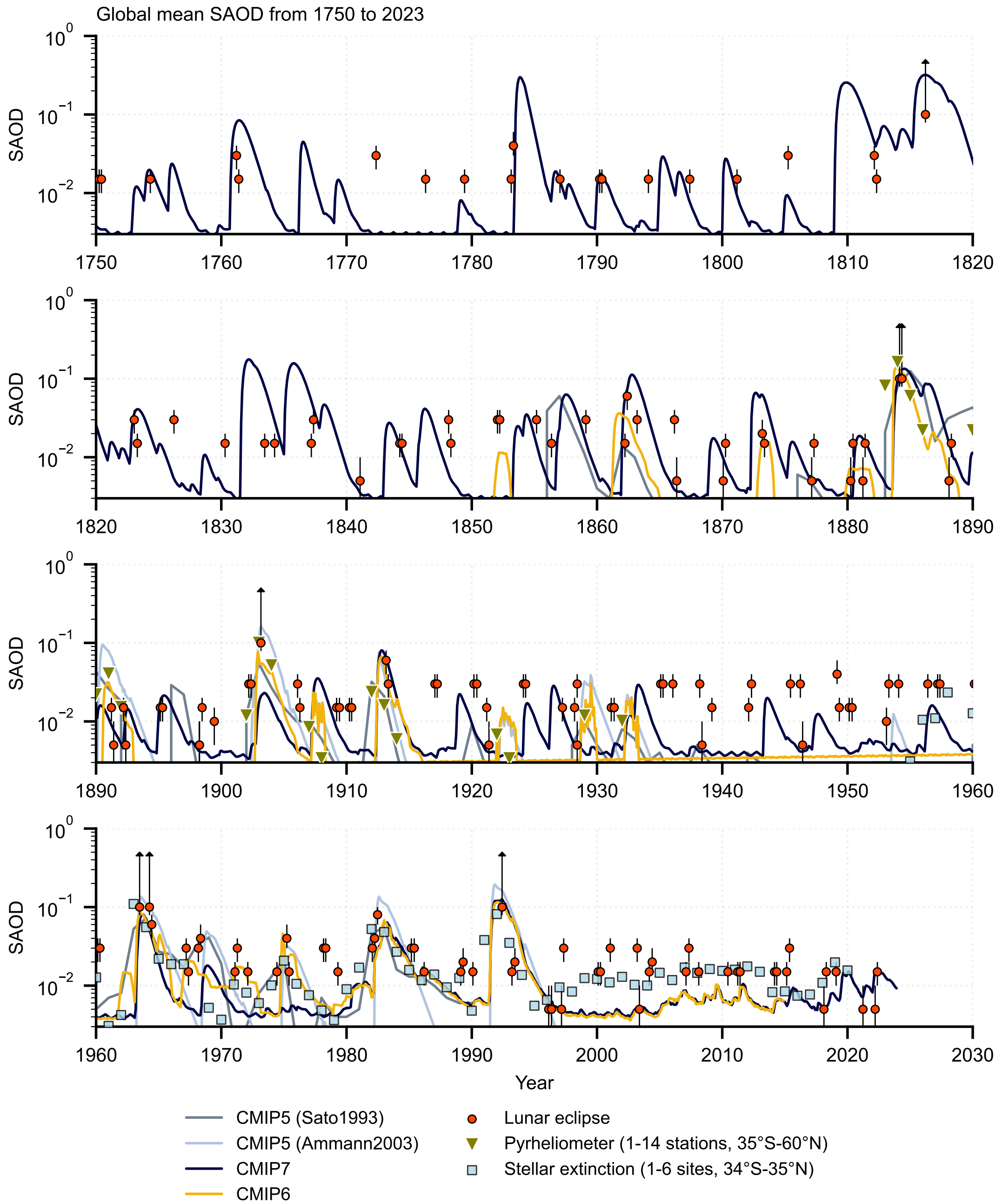

Figure 2. Global-mean stratospheric aerosol optical depth (SAOD, log scale) from 1750 to 2023, comparing CMIP5, CMIP6, and CMIP7 forcing datasets with observational estimates. The observations are from lunar eclipse data from Boissel and Guillet (2026), pyrheliometric measurements from Stothers (1996), and stellar extinction data from Rodgers and Toohey (2026). An upward arrow indicates lunar eclipse data that do not have an upper bound on the SAOD range ($L = 0$).

https://doi.org/10.5194/egusphere-2026-4193
Preprint. Discussion started: 23 July 2026

We compare the global-mean SAOD time series across CMIP5, CMIP6, and CMIP7 forcing datasets, along with observations from lunar eclipses, pyrheliometric measurements, and stellar extinction data in Figure 2.

The CMIP7 forcing dataset represents major methodological changes over CMIP6, leading to substantial differences in SAOD. The global-mean SAOD averaged over the historical period is 0.0107 for CMIP6 (1850–2014) and 0.0135 for CMIP7 (1850–2021). The greater SAOD magnitude in CMIP7 arises from the addition of small-to-moderate magnitude eruptions in the pre-satellite era (1850–1978) in CMIP7 using volcanic SO_2 emissions from a geological database (Global Volcanism Program, 2025) and a high-resolution ice-core dataset (Fang et al., 2023). CMIP7 yields a more coherent SAOD time series over the full historical period than CMIP6, with more similar frequencies of small-to-moderate magnitude eruptions between the satellite and pre-satellite era.

Observations independent of the CMIP7 dataset, including pyrheliometric measurements, lunar eclipses, and stellar extinction data, are valuable for validating SAOD especially in the pre-satellite period. Volcanic emissions derived from ice cores have a high uncertainty in SO_2 mass, especially after 1900 since increased anthropogenic sulfur emissions masked the ice-core volcanic sulfate signals, thus making independent observations important for forcing validation. We find that CMIP7 has years without matching SAOD peaks when independent observations show SAOD values greater than 0.01. For instance, pyrheliometric measurements, lunar eclipses, and stellar extinction data indicate SAOD perturbations in years 1921, 1929, and 1974 that are not captured in CMIP7 (Fig. 2). This suggests that the CMIP7 volcanic emission inventory may be missing or underestimating SO_2 emissions for some eruptions.

However, the SAOD estimates derived from independent observations are also subject to uncertainties. For instance, both lunar eclipses and stellar extinction data show higher SAOD estimates than the satellite observations between 1997 and 2015 (Fig. 2). Lunar eclipse data for luminosity classes with $L \geq 1$ are subject to greater uncertainties due to differences in observer experience and atmospheric conditions (see Sect. 2.3.1). For stellar extinction data, there is a lack of available measurements in the SH from 1995 onwards (Fig. S2b). The stellar-extinction-derived SAOD over the NH shows good agreement with GloSSAC data (Fig. S2a) but the global-mean values are higher than those in CMIP7 (Fig. 2), likely due to biases introduced by averaging over NH data only due to the lack of SH stations.

In Section 3.1.5, we compare the SAOD of selected major eruptions with independent observation data for further evaluation of individual eruption cases.

3.1.2 Climatologies of SAOD in CMIP7 and CMIP6

The climatologies of the extinction coefficient, which yields SAOD when vertically integrated, show only small variations in magnitude between CMIP6 and CMIP7, especially for the annual mean (Fig. 3). The CMIP7 annual climatology shows a stronger increase in extinction towards high latitudes in the lower stratosphere. In CMIP6, there is a more pronounced decrease in extinction above the tropopause in the tropics and subtropics, which is confined to the SH subtropics in CMIP7. Aside from these differences, the latitude–altitude profiles are very similar and show a decrease in extinction with increasing altitude. From month to month, there are more differences in the latitudinal profile in CMIP6, while extinction remains fairly similar across months in CMIP7. For example, CMIP7 shows consistently high extinction in the NH high latitudes, a signal which appears

https://doi.org/10.5194/egusphere-2026-4193
Preprint. Discussion started: 23 July 2026

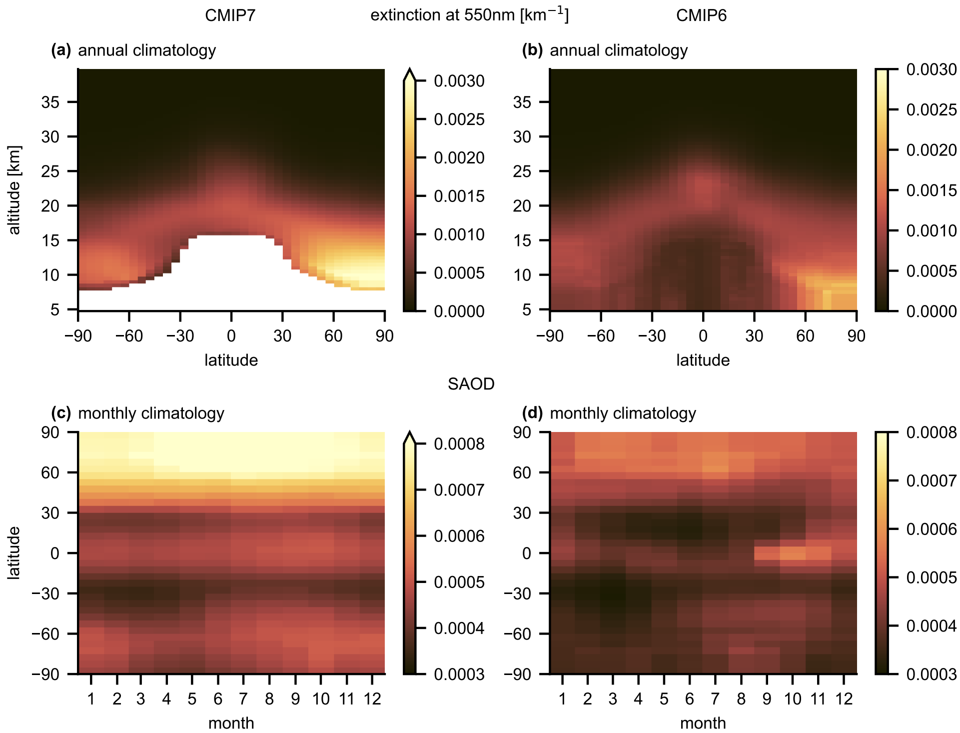

Figure 3. Comparison of annual (a, b) and monthly climatologies (c, d) of the extinction coefficient at 550 nm in CMIP7 (left column) and CMIP6 (right column). The climatologies cover data from 1850 to 2014 (CMIP6)/2021 (CMIP7).

only between March and July in CMIP6 and is overall less pronounced there. CMIP6 exhibits notably low extinction across latitudes, especially during the first half of the year, while CMIP7 shows more variations between latitudes.

3.1.3 Frequency–magnitude distribution of SO_2 emission and SAOD

The CMIP7 volcanic sulfur emissions dataset documents a total of 463 explosive eruptions, including 317 eruptions in the satellite period (1979–2021) and 146 eruptions in the pre-satellite period (1750–1978; Aubry et al., 2026a). A key limitation of the CMIP6 stratospheric aerosol forcing dataset was the under-representation of small-to-moderate magnitude eruptions in the pre-satellite era. To address this gap, the CMIP7 volcanic sulfur emissions dataset includes 69 small-magnitude eruptions recorded in the GVP geological database with Volcanic Explosivity Index (VEI) of 4 and 5 that were not captured in ice-core records (Aubry et al., 2026a). These eruptions constitute about 50% of the CMIP7 pre-satellite eruptions and are assigned SO_2 emission values of 0.08 Tg and 2.78 Tg for VEI 4 and VEI 5 eruptions, respectively (Fig. 4a). A previous study shows that the CMIP6 1850–2014 mean SAOD value (0.0107) is biased low compared to the SAOD distribution generated by statistical resampling of eruptions in the past 11,500 years, largely because it does not account for small-to-moderate magnitude eruptions

https://doi.org/10.5194/egusphere-2026-4193
Preprint. Discussion started: 23 July 2026

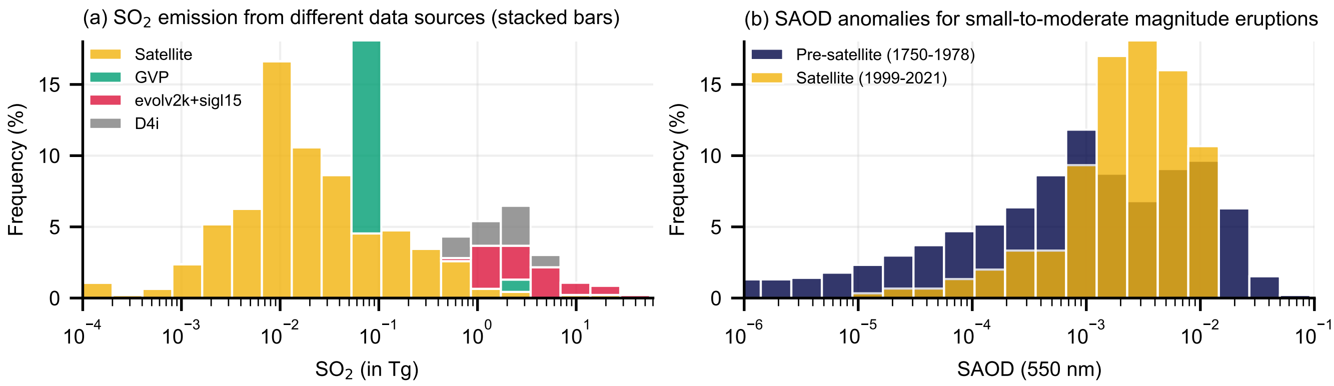

Figure 4. Frequency–magnitude distributions for (a) volcanic SO_2 emissions from different data sources (shown as stacked bars), (b) monthly-mean CMIP7 stratospheric aerosol optical depth (SAOD) anomalies for small-to-moderate magnitude eruptions in the pre-satellite period (1750–1978, without background non-volcanic stratospheric aerosols) and satellite period (1999–2021, relative to the minimum value of year 1998).

before 1978 (Chim et al., 2023). CMIP7 includes more small-to-moderate magnitude eruptions in the pre-satellite era, which is consistent with observations from the lunar eclipse dataset (Fig. 2).

Despite these improvements, the frequency–magnitude distributions reveal limitations of the CMIP7 dataset. Figure 4 shows the distributions of CMIP7 volcanic SO_2 emissions and the monthly-mean SAOD anomalies in the pre-satellite (1750–1978) and satellite (1999–2021) periods for small-to-moderate magnitude eruptions. Despite the inclusion of additional small-to-moderate magnitude eruptions from the GVP geological database and the D4i high-resolution Greenland ice core, there are more months in the pre-satellite period (55%) with SAOD values lower than 10^{-3} as compared to the satellite period (28%). This suggests that the CMIP7 dataset likely underestimates the SAOD contribution from small-magnitude eruptions in the pre-satellite period.

3.1.4 Non-volcanic background aerosols

Stratospheric aerosol forcing in CMIP6 and CMIP7 includes non-volcanic background aerosols, which are derived using the same methodology (Luo, 2018; Aubry et al., 2026b), while in CMIP5, the volcanic forcing datasets from Ammann et al. (2003) and Sato et al. (1993) do not include non-volcanic background aerosols. CMIP6 and CMIP7 derive the non-volcanic background aerosols from the climatological mean of a relatively volcanically quiescent period in the satellite era, and scale the SAOD using the non-volcanic stratospheric sulfate aerosol burden simulated by Sheng et al. (2015). The reference periods of the volcanically quiescent years in CMIP6 and CMIP7 are 1999–2005 and 1998–2001, respectively, with mean values of 0.0045 and 0.0044. CMIP7 uses the period 1998–2001 to avoid the influence of three small-magnitude eruptions in 2002 (Ruang, Etna, and Reventador), but the differences in the means are small. The non-volcanic background aerosol forcing in CMIP7 is consistently higher than that of CMIP6 during pre-satellite volcanically quiescent periods and exhibits a much greater

https://doi.org/10.5194/egusphere-2026-4193
Preprint. Discussion started: 23 July 2026

seasonal cycle (Fig. S3, S14). The amplitude of the seasonal cycle in CMIP7, although small in absolute values, increased by about 30% between 1850 and 1950. We also find that the SAOD trend in CMIP6 is not linear, while CMIP7 shows a linear trend in the non-volcanic background aerosols (Fig. S3a).

3.1.5 Selected major eruptions

Figure 5 shows the zonal-mean aerosol extinction as a function of altitude and latitude for the seven largest pre-satellite eruptions in CMIP6, which were simulated using the AER2D model, and the comparison against CMIP7. For the remainder of this section, we focus on five of these eruptions in the pre-satellite era with significant differences in SAOD magnitude or distribution for detailed comparison with independent observations, including the 1861 unidentified eruption (possibly Mt. Kie Besi), 1883 Krakatau, 1902 Santa María, 1963 Agung, and 1974 Fuego eruptions. We also examine the two largest satellite-era eruptions, 1982 El Chichón and 1991 Mt. Pinatubo.

For each eruption examined subsequently, we compare the CMIP6 and CMIP7 SAOD at 550 nm over the latitude band for which pyrheliometer, stellar extinction, and lidar data are available. For each latitude band, we show the minimum and maximum SAOD, with shading in between (i.e., the shading represents the SAOD range within a latitude band, not uncertainty). Note that comparisons are not always like-for-like. Lunar eclipses and lidar data are instantaneous rather than monthly means, even though we bin lidar data to monthly resolution. Stellar extinction, pyrheliometer, and lidar data represent pointwise measurements and thus should be compared to the 5°-binned CMIP7 data with caution. For eruptions prior to the pyrheliometric measurement period, only SAOD derived from lunar eclipse observations is available for comparison, which represents the global-mean rather than the hemispheric-mean SAOD, although there is typically some weighting toward one hemisphere, depending on the eclipse path (Keen, 1983). For post-1979 eruptions, where both CMIP6 and CMIP7 use GloSSAC, we also compare against other satellite datasets and to what EVA_H would have simulated.

https://doi.org/10.5194/egusphere-2026-4193
Preprint. Discussion started: 23 July 2026

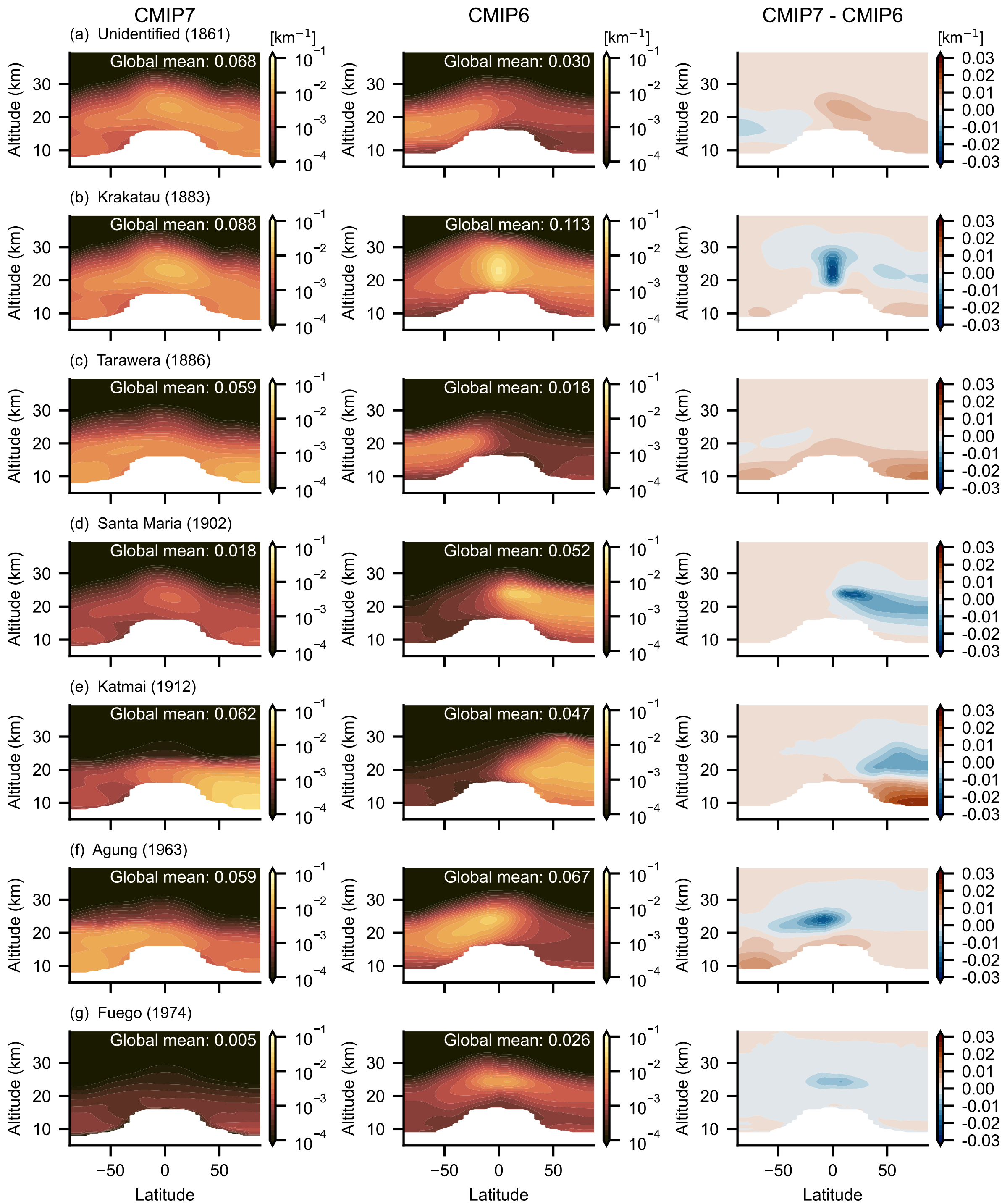

Figure 5. Zonal-mean stratospheric aerosol extinction from CMIP7, CMIP6, and their differences, averaged over the 12 months following each eruption: (a) Unidentified eruption (1861), (b) Krakatau (1883), (c) Tarawera (1886), (d) Santa María (1902), (e) Katmai (1912), (f) Agung (1963), and (g) Fuego (1974).

https://doi.org/10.5194/egusphere-2026-4193
Preprint. Discussion started: 23 July 2026

The 1861 eruption, for which no definitive source has been identified, shows a significant difference in aerosol distribution and SAOD magnitude between CMIP6 and CMIP7. The eruption is classified as an unknown SH eruption in CMIP6, and attributed to a VEI 4 tropical eruption of Mt. Kie Besi in CMIP7 with 9 Tg SO_2 injection. Another large tropical eruption at Dubbi volcano in Eritrea erupted in May 1861 (Wiart and Oppenheimer, 2000), representing an alternative candidate for this unidentified event. These different eruption latitudes result in distinct zonal aerosol distributions between CMIP6 and CMIP7, with CMIP7 showing a higher SAOD over the NH (Fig. 5). The global-mean SAOD is significantly higher in CMIP7 than in CMIP6 (Fig. 6a), with the 12-month-averaged global-mean SAOD following the eruption being more than double in CMIP7 (0.068) compared to CMIP6 (0.03), though CMIP7 includes an additional eruption (Bárðarbunga, Iceland) in 1862 that contributes to the SAOD increase. Neither the CMIP6 nor CMIP7 global-mean SAOD values fall within the range of SAOD estimates derived from lunar eclipses (Fig. 6a).

The 1883 Krakatau eruption has 19 Tg SO_2 injection in CMIP7. The peak global-mean SAOD exhibits a comparable magnitude between CMIP6 and CMIP7 (Fig. 5), while the global-mean SAOD averaged over 12 months following the eruption is lower in CMIP7 (0.088) than in CMIP6 (0.113). This SAOD reduction occurs mainly over the tropics (Fig. 5b). The SAOD reached its peak value after 3 months in CMIP6 and after 11 months in CMIP7 (Fig. 6b). This difference reflects the different aerosol transport processes and production timescales in the two models, with the EVA_H reduced-complexity model reaching the peak SAOD slower than the AER2D model.

Three tropical eruptions occurred in 1902, with Santa María alone injecting 2 Tg SO_2 into the stratosphere in CMIP7 (Fig. 7). The difference between CMIP generations is striking: the NH SAOD peaks at 0.14 in CMIP6, while it does not exceed 0.03 in CMIP7. Pyrheliometric and lunar eclipse data support an SAOD exceeding 0.1 in the NH mid-latitudes, indicating that CMIP7 likely underestimates the extinction by a large margin. In the SH, both CMIP datasets agree on a peak extinction of around 0.02, but no pyrheliometer data are available (not shown).

The two Agung eruptions in 1963 injected a total of 10 Tg SO_2 into the stratosphere in CMIP7. The global-mean SAOD averaged over the 12 months following the eruption is comparable between CMIP7 (0.059) and CMIP6 (0.067). The aerosols are concentrated mostly over the SH in the first post-eruption year, though CMIP7 exhibits slightly lower SAOD over the SH mid-latitudes than CMIP6 (Fig. 5f). The apparent delayed increase in SAOD over the NH in CMIP6 appears to match the stellar extinction data better than CMIP7, although lunar eclipse and lidar data suggest higher SAOD values than CMIP6 in 1964 (Fig. 8a). For the SH, the stellar extinction data matches CMIP6 better in the first 6 months after the eruption than CMIP7 (Fig. 8). Notably, stellar extinction data, lunar eclipse data, lidar measurements, searchlight data, and CMIP6 show small SAOD peaks in July 1964 and January 1965 in the SH and between April and July 1965 over the NH, none of which are captured by CMIP7. Although CMIP7 includes a VEI 4 eruption in 1964 from Sheveluch (57°N), it is unlikely that this high-latitude NH eruption is the source of SAOD increase in the SH within three months following the eruption, suggesting that there is a potential missing eruption in late 1964 or early 1965 in the CMIP7 volcanic sulfur emission dataset.

The 1974 Fuego eruption is a VEI 4 eruption with an assigned SO_2 injection of 0.08 Tg in CMIP7. The eruption has a significantly lower global-mean SAOD averaged over the 12 months following the eruption in CMIP7 (0.005) compared to CMIP6 (0.026) (Fig. 5g). The SAOD in CMIP7 for both hemispheres is close to background levels (Fig. 9). Both stellar

https://doi.org/10.5194/egusphere-2026-4193
Preprint. Discussion started: 23 July 2026

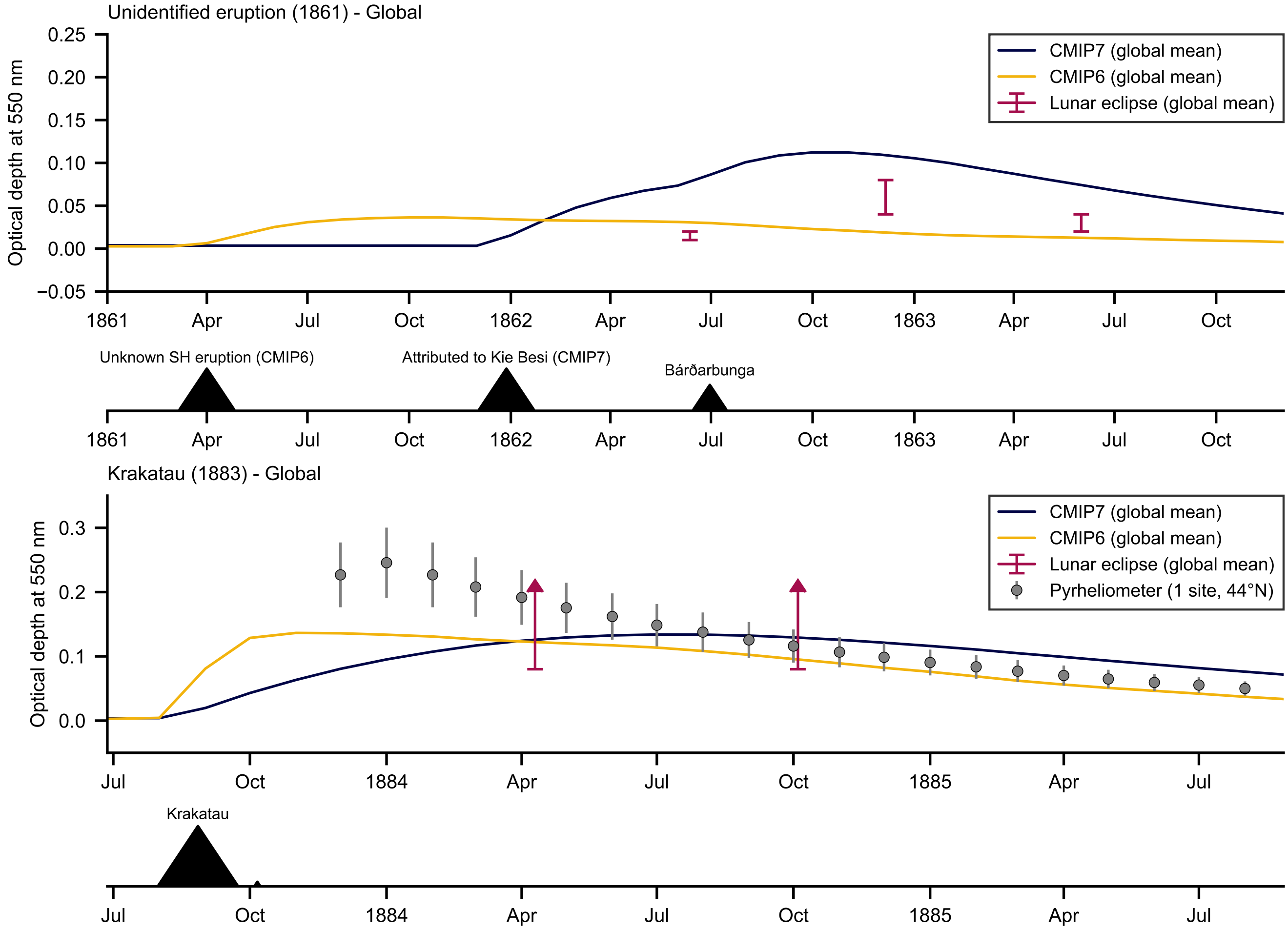

Figure 6. Global-mean aerosol optical depth (at 550 nm) for the 1861 unidentified eruption attributed to Mt. Kie Besi eruption in CMIP7 (0°), and the 1883 Krakatau eruption (6°S). Lunar eclipse data are obtained from Boissel and Guillet (2026). The upward arrow indicates that the lunar eclipse data do not have an upper bound on the SAOD range ($L = 0$). Pyrheliometric data are from Stothers (1996) at Montpellier (44°N).

extinction and lunar eclipse derived SAOD estimates suggest a higher SAOD range than background levels, which matches better with CMIP6 values. CMIP7 likely underestimates volcanic sulfur emissions from the 1974 Fuego eruption, leading to an underestimation of SAOD.

The 1982 El Chichón eruption injected 7 Tg SO_2 in CMIP7, accompanied by minor eruptions of Galunggung (Fig. 10). The NH CMIP7 SAOD in the six months following the eruption is much lower (peak at 0.05) than indicated by lidar (peak at 0.25) and stellar extinction data (peak at 0.15). Particularly the lidar data from Mauna Loa, which is at a similar latitude as El Chichón, show a very strong peak around three months after the eruption. The discrepancy with CMIP7 is due to a gap in global satellite data for 1982–1984 between the SAGE and SAGE II missions, which has been filled in GloSSAC based

https://doi.org/10.5194/egusphere-2026-4193
Preprint. Discussion started: 23 July 2026

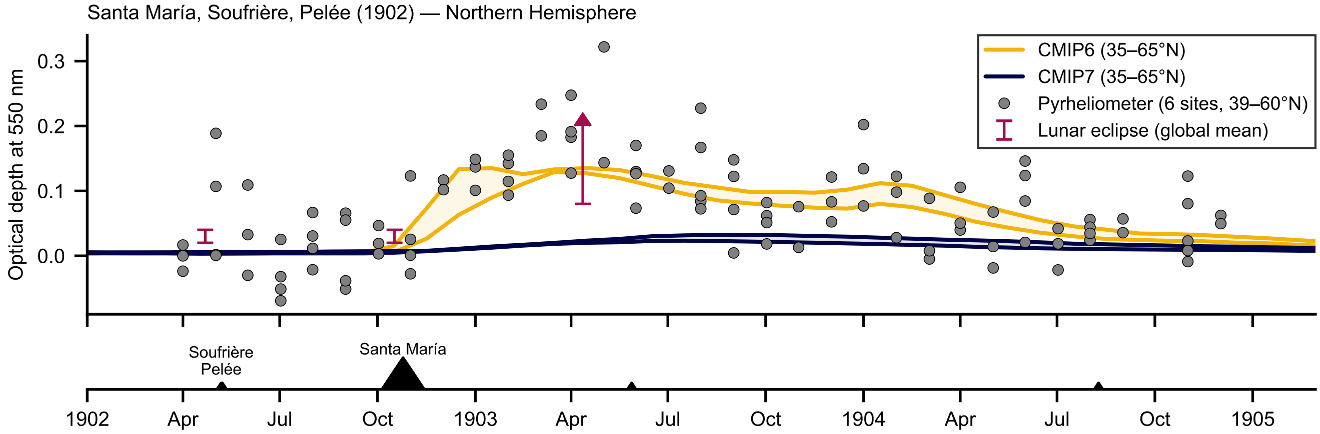

Figure 7. Northern Hemisphere aerosol optical depth (at 550 nm) for the 1902 Santa María, Soufrière St. Vincent, and Pelée eruptions (all 14°N). Lunar eclipse data from Boissel and Guillet (2026). Pyrheliometer data are from Stothers (1996) for Pavlovsk (60°N), Potsdam (52°N), Warsaw (52°N), Clarens/Lausanne (46°N), Monte Cimone (44°N), and Washington, DC (39°N). The upward arrow indicates that the lunar eclipse data do not have an upper bound on the SAOD range ($L = 0$). The shading shows the CMIP6 and CMIP7 SAOD ranges between the latitude bands indicated in the legend.

on high-latitude satellite data and NH mid-latitude ground-based and airborne lidar data (Thomason et al., 2018; also see Fig. 4.4 of SPARC, 2006), which do not include the Mauna Loa lidar data shown here. The zonal-mean structure of SAOD thus also appears discontinuous due to the way sparse lidar measurements are extrapolated to other latitudes (Fig. 10c), and there are vertical discontinuities (Fig. 10d). Lunar eclipse data, however, support a low extinction in 1982, and the hemispheric and global means may be better than the pointwise lidar data suggest, although this cannot be corroborated without more expansive data coverage. Starting in 1983, all data sources agree on an NH SAOD of 0.05–0.15. The EVA_H model simulates a matching SAOD in the SH based on only the emission parameters, but the simulated NH SAOD is smoother and lower than suggested by CMIP and observational data.

https://doi.org/10.5194/egusphere-2026-4193
Preprint. Discussion started: 23 July 2026

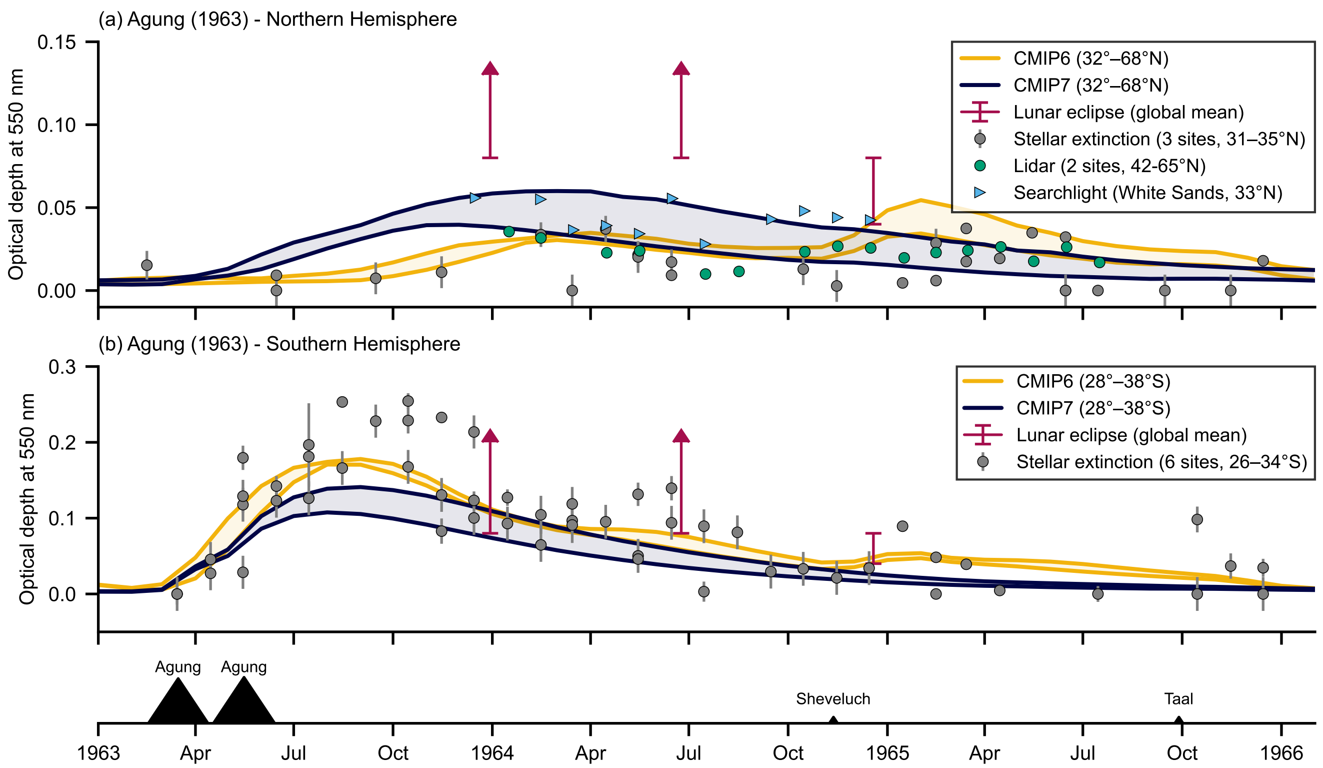

Figure 8. (a) Northern Hemisphere and (b) Southern Hemisphere aerosol optical depth (at 550 nm) for the 1963 Agung eruption (8°S). Lunar eclipse data are obtained from Boissel and Guillet (2026). Stellar extinction data are from Rodgers and Toohey (2026) for Flagstaff (35°N), Mount Locke (31°N), Kitt Peak (32°N), Mount Bingar (34°S), Sutherland (32°S), Cerro Tololo (30°S), La Silla (29°S), Bloemfontein (29°S), and Pretoria (26°S). Lidar and searchlight data are from Antuña-Marrero et al. (2020a) and Antuña-Marrero et al. (2023) for White Sands (33°N), Lexington (42°N), and Fairbanks (65°N). The upward arrow indicates that the lunar eclipse data do not have an upper bound on the SAOD range ($L = 0$). The shading shows the CMIP6 and CMIP7 SAOD ranges between the latitude bands indicated in the legend.

https://doi.org/10.5194/egusphere-2026-4193
Preprint. Discussion started: 23 July 2026

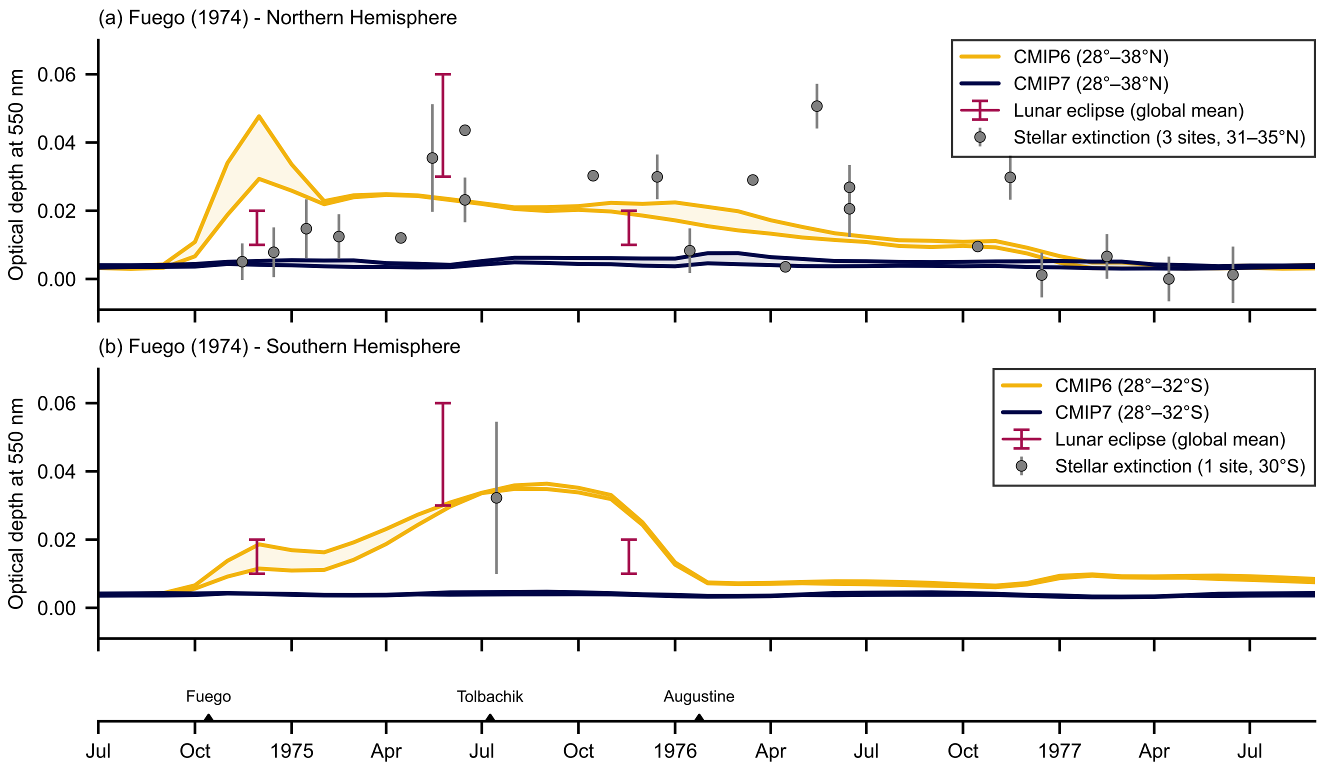

Figure 9. (a) Northern Hemisphere and (b) Southern Hemisphere aerosol optical depth (at 550 nm) for the 1974 Fuego eruption (14°N). Lunar eclipse data are obtained from Boissel and Guillet (2026). Stellar extinction data are from Rodgers (2022) for Flagstaff (35°N), San Pedro Mártir (31°N), Mount Locke (31°N), and Cerro Tololo (30°S). The shading shows the CMIP6 and CMIP7 SAOD ranges between the latitude bands indicated in the legend.

https://doi.org/10.5194/egusphere-2026-4193
Preprint. Discussion started: 23 July 2026

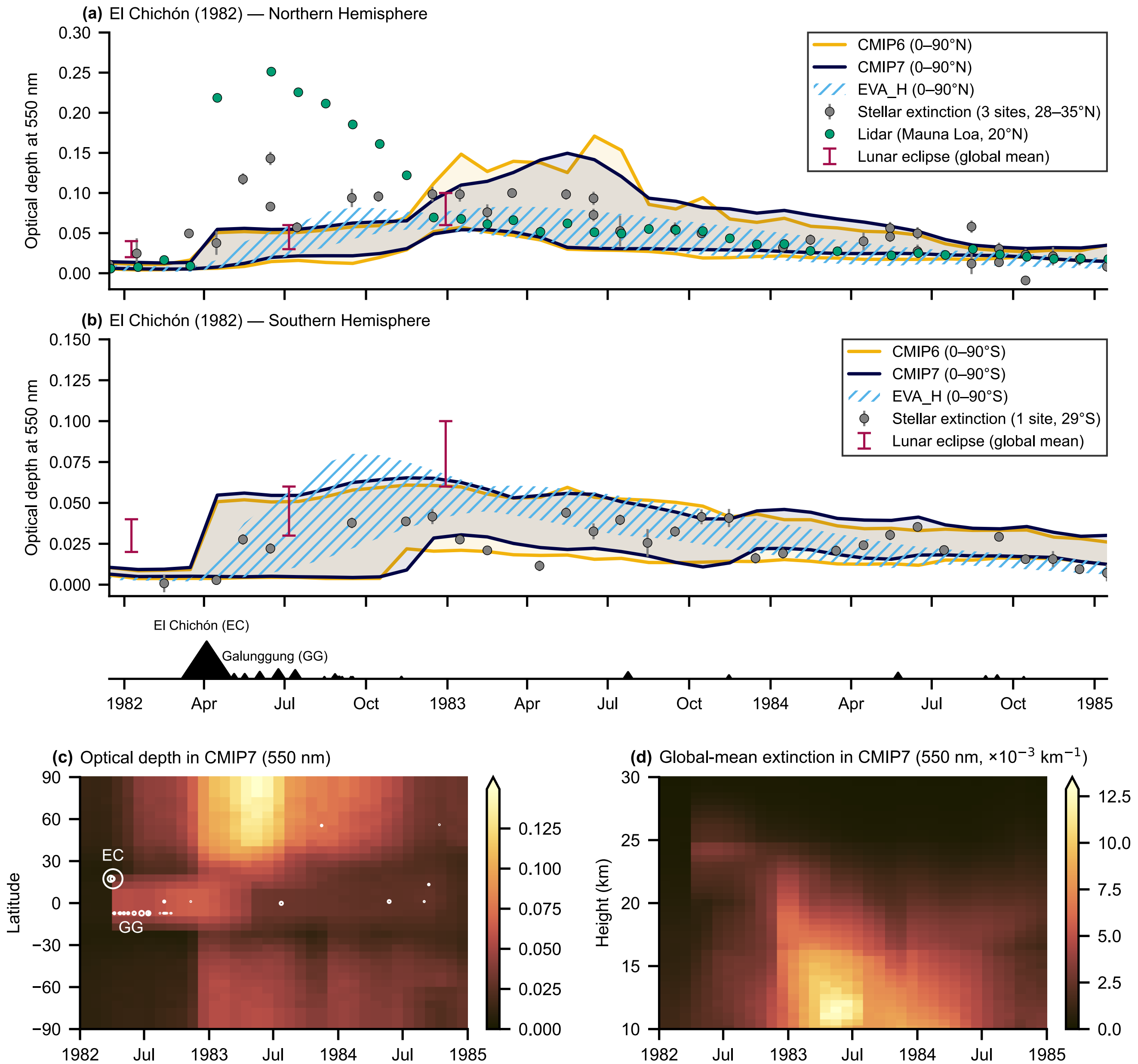

Figure 10. (a) Northern Hemisphere and (b) Southern Hemisphere aerosol optical depth (at 550 nm) for the 1982 El Chichón (17°N) and Galunggung (7°S) eruptions. (c) Zonal-mean optical depth and (d) global-mean extinction in CMIP7. Lunar eclipse data are obtained from Boissel and Guillet (2026). Stellar extinction data are from Rodgers (2022) for Canary Islands (28°N), San Pedro Mártir (31°N), Flagstaff (35°N), and La Silla (29°S). Error bars denote the standard error of the mean. Lidar data are from Mauna Loa (John E. Barnes, pers. comm.). White circles in (c) indicate volcanic eruptions scaled by injected SO_2 mass. The shading shows the CMIP6 and CMIP7 SAOD ranges between the latitude bands indicated in the legend.

https://doi.org/10.5194/egusphere-2026-4193
Preprint. Discussion started: 23 July 2026

The 1991 Mt. Pinatubo eruption was the largest eruption of the 20th century, with an injection of 15 Tg SO_2 estimated in CMIP7. Accurate forcing for Pinatubo is critical since it is often taken as representative of large magnitude eruptions in coordinated modelling experiments (e.g., Zanchettin et al., 2016) and mechanistic studies (e.g., Pauling et al., 2021; Dogar et al., 2020). However, aerosol extinction was so strong in the lower tropical and subtropical stratosphere after Pinatubo that SAGE II measurements were not possible, resulting in a gap from June 1991 until the end of 1993 (SPARC, 2006). This gap is filled in GloSSAC using ground-based lidar data from the subtropics for June–September 1991 and other satellite instruments (CLAES and HALOE) after October 1991 (Thomason et al., 2018; Kovilakam et al., 2020).

Figure 11 shows the SAOD following the 1991 Mt. Pinatubo eruption. All satellite-based datasets, including CMIP, agree that the NH mid-latitude SAOD peaked at around 0.1 starting three months after the eruption and persisting for about 15 months (Fig. 11a). It is particularly encouraging that the stellar extinction data also match well, although the CREST merged satellite dataset, which uses a different method to fill the gap and was interpolated to 550 nm using the Ångström formula, has a slightly lower peak SAOD (0.09) than CMIP7 (0.12) averaged over the NH mid-latitudes. In contrast, the lidar data (Fig. 11b) indicate much higher extinctions, possibly exceeding 0.3, and a wider spread of transport timescales across latitudes. However, uncertainties in the lidar data due to the extinction-to-backscatter ratio and wavelength conversions are large so that the lidar extinctions could reasonably be 50% smaller. The agreement between CMIP7, CMIP6, and CREST in the SH is similar to the NH, although the stellar extinction data point to a slightly lower SAOD (Fig. 11c). The EVA_H model aligns with the satellite data in the NH, but does not capture the dip in SH SAOD in the first year following the eruption.

3.1.6 CMIP7 comparison with satellite datasets

After 1979, the CMIP7 dataset is based on extinctions from GloSSAC. We compare the SAOD in CMIP7 derived from these extinctions with CREST and OMPS-LP. For comparison, the relative difference is defined as the difference divided by the mean of two datasets.

CREST (Sofieva et al., 2024b) is a merged record of SAOD at 750 nm from multiple satellite instruments. It relies on much of the same observations as GloSSAC, but adds additional satellite data (including OMPS-LP after 2012, compared next) and processes observations differently. The zonal-mean SAOD over 1985–2023 is shown in Figure 12. CREST agrees closely with CMIP7 over much of the record, with a median difference of 5%. CREST has a higher SAOD than CMIP7 everywhere except for the subtropics. The 1991 Mt. Pinatubo eruption has a similar zonal structure but a larger extinction in CMIP7. This mismatch for the Mt. Pinatubo eruption is likely due to the way the two datasets account for gaps due to instrumental saturation of SAGE II during this period (Sofieva et al., 2024b): CREST fits an empirical function, while GloSSAC incorporates other satellite observations and ground-based lidar data. Larger differences also exist for a number of NH high-latitude eruptions (e.g., 2008 Kasatochi, 2009 Sarychev, 2019 Raikoke); the agreement for the 2022 Hunga Tonga–Hunga Ha'apai eruption is good (Fig. S12).

OMPS-LP (Rozanov et al., 2024) data were not included in GloSSAC and thus enable independent validation. OMPS-LP provides retrievals of extinction at 869 nm, while extinction at this wavelength is derived from Mie theory in CMIP7 based on the 525-nm extinction and the 525-to-1020-nm extinction ratio in GloSSAC. The zonal-mean SAOD over 2012–2023 is

https://doi.org/10.5194/egusphere-2026-4193
Preprint. Discussion started: 23 July 2026

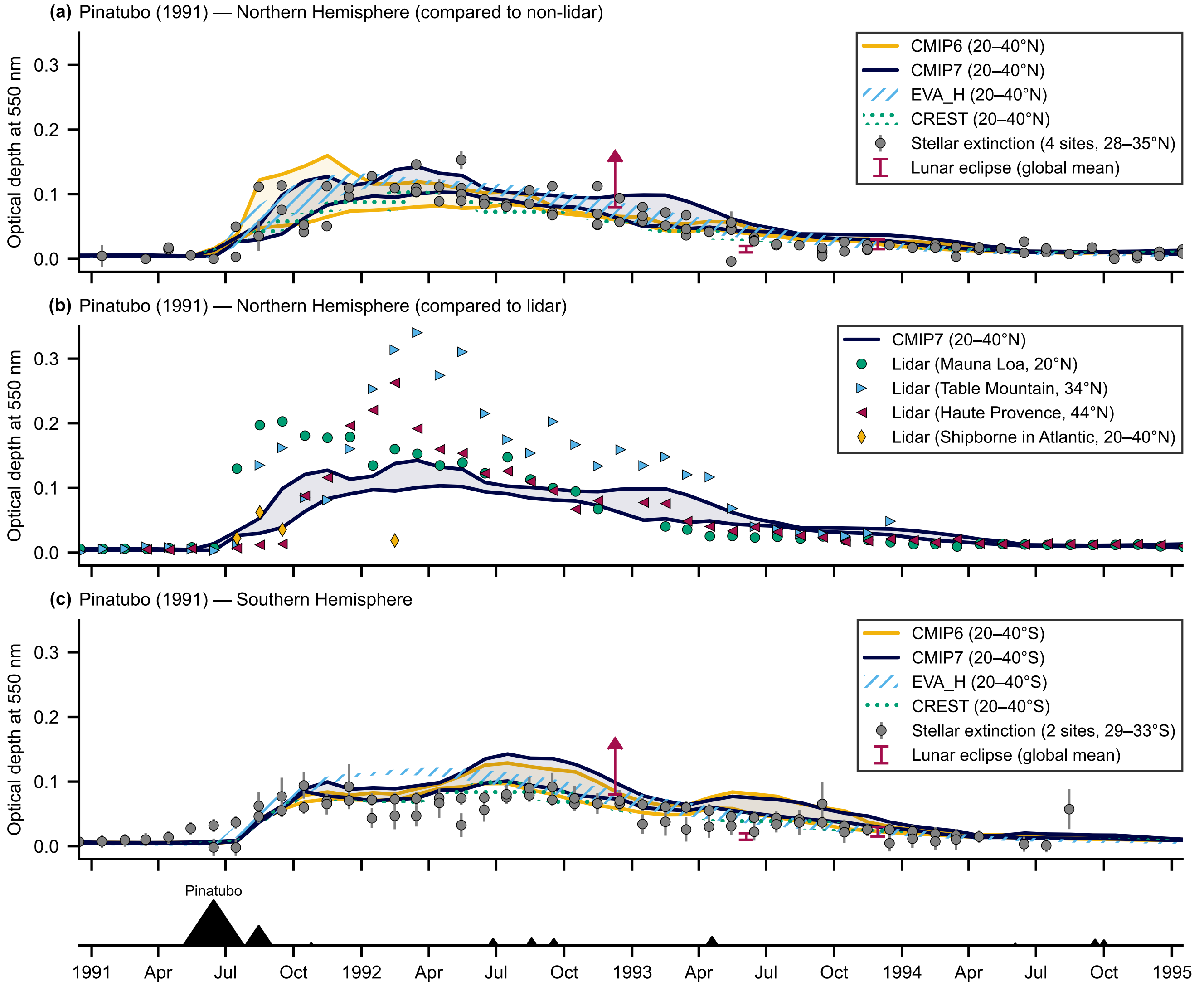

Figure 11. (a, b) Northern Hemisphere and (c) Southern Hemisphere aerosol optical depth (at 550 nm) for the 1991 Mt. Pinatubo eruption (15°N). Lunar eclipse data are obtained from Boissel and Guillet (2026). Stellar extinction data are from Rodgers (2022) for Washington Camp (31°N), Canary Islands (28°N), San Pedro Mártir (31°N), Flagstaff (35°N), La Silla (29°S), and Sutherland (32°S). Error bars denote the standard error of the mean. Shipborne lidar data are from Antuña-Marrero et al. (2020c). Ground-based lidar data are from Mauna Loa (John E. Barnes, pers. comm.), Table Mountain, California (Thierry Leblanc, pers. comm.), and Haute-Provence (Sergey M. Khaykin, pers. comm.). The upward arrow indicates that the lunar eclipse data do not have an upper bound on the SAOD range ($L = 0$). The shading shows the CMIP6 and CMIP7 SAOD ranges between the latitude bands indicated in the legend.

shown in Figure 13. Although the two datasets agree qualitatively, the median difference is 9% before 2022. CMIP7 has a persistently lower SAOD in the mid- and high latitudes, although OMPS-LP has a higher SAOD in the subtropics, particularly

https://doi.org/10.5194/egusphere-2026-4193
Preprint. Discussion started: 23 July 2026

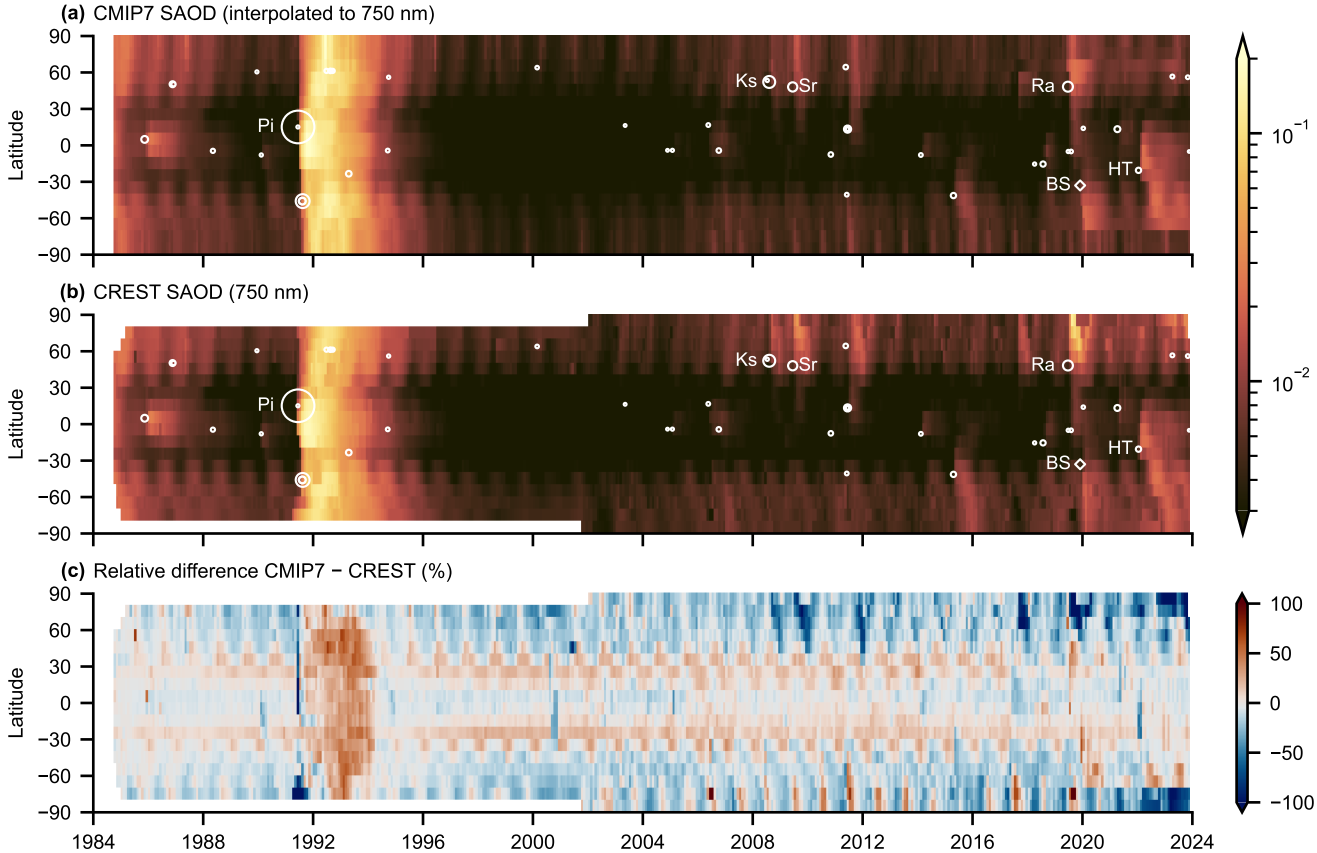

Figure 12. Stratospheric aerosol optical depth in CMIP7 and CREST satellite observations at 750 nm. The CMIP7 5° data were binned to the CREST 10° latitude grid. The monthly climatological tropopause from CMIP7 is applied to CREST. The 1991 Mt. Pinatubo (Pi), 2008 Kasatochi (Ks), 2009 Sarychev (Sr), 2019 Raikoke (Ra), and 2022 Hunga Tonga–Hunga Ha'apai (HT) eruptions are mentioned in the text. White circles indicate volcanic eruptions exceeding 0.5 Tg SO_2, scaled by injected SO_2 mass. The white diamond in December 2019 represents the Black Summer (BS) Australian pyrocumulonimbus.

in the SH. Such biases may be caused by wavelength conversions, location-dependent influence of particle-size assumptions, and possibly by differences in vertical extinction profiles. The OMPS-LP observation geometry also affects errors: in the SH, the scattering angle between the instrument's line of sight and the sun is larger than in the NH, which reduces aerosol sensitivity and increases SH uncertainties in the OMPS-LP extinction retrievals. The difference increases after the Hunga Tonga–Hunga Ha'apai eruption in January 2022. In CMIP7, the HT plume onset appears delayed by one month, likely because SAGE III (GloSSAC's primary instrument in this period) has fewer observations of the HT plume in January and February 2022 than OMPS-LP (cf. Fig. 3 in Bourassa et al., 2023). The delayed onset is also evident in the comparison with CREST (Fig. S12). The peak extinction for HT is lower in OMPS-LP than in CMIP7, although CREST and CMIP7 agree at 750 nm (Fig. S11, S12). Since CREST is mainly based on OMPS-LP during this period, the bias is likely due to the wavelength conversion or CREST's

https://doi.org/10.5194/egusphere-2026-4193
Preprint. Discussion started: 23 July 2026

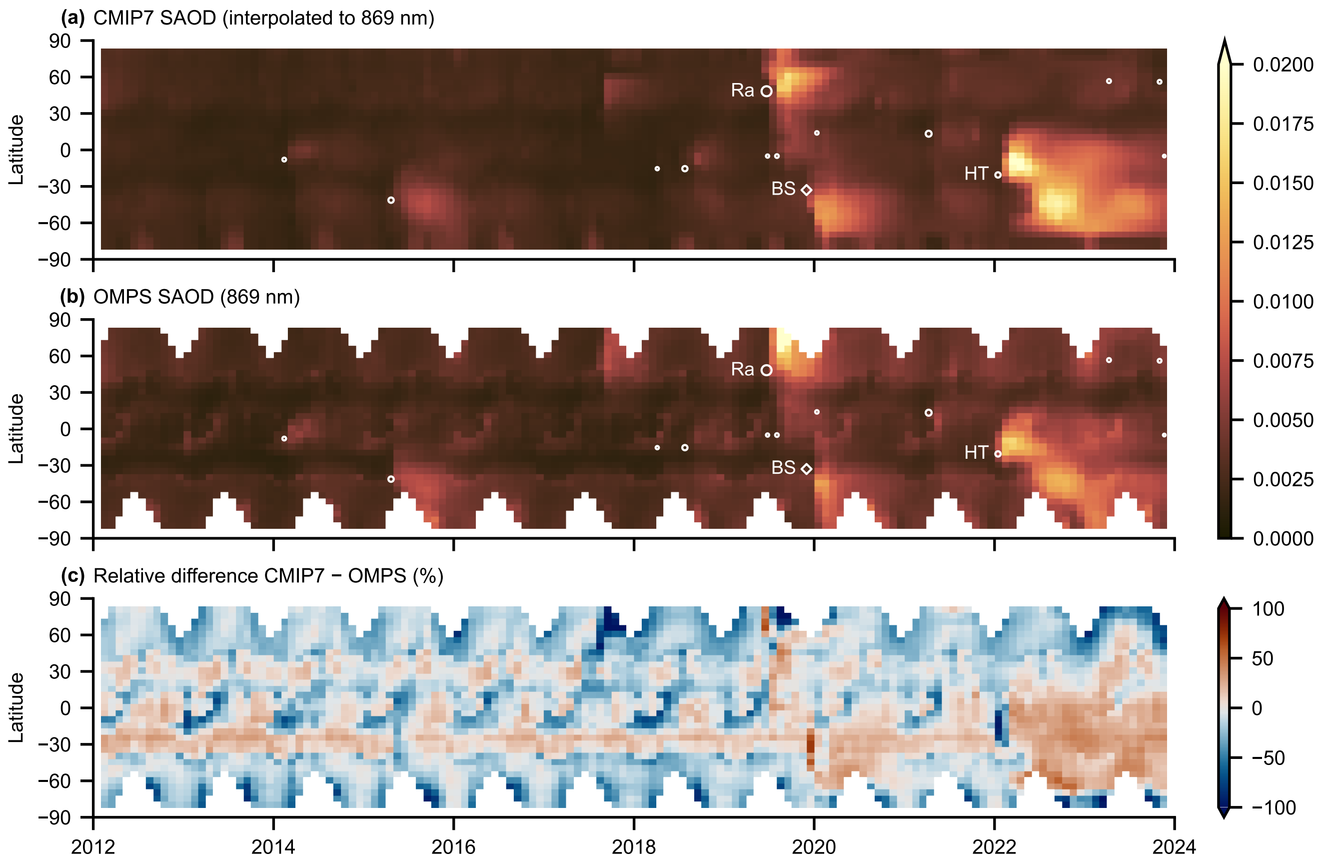

Figure 13. Stratospheric aerosol optical depth in CMIP7 and OMPS-LP satellite observations at 869 nm. The CMIP7 data were linearly interpolated to the OMPS-LP latitude grid. Extinction below 12 km is excluded, and the monthly climatological tropopause from CMIP7 is applied to OMPS-LP. The 2022 Hunga Tonga–Hunga Ha'apai (HT) eruption is mentioned in the text. White circles indicate volcanic eruptions exceeding 0.05 Tg SO_2, scaled by injected SO_2 mass. The white diamond in December 2019 represents the Black Summer (BS) Australian pyrocumulonimbus.

merging approach. Large differences among OMPS-LP retrievals and compared to other satellite instruments for HT have been noted before, and can be attributed to the fixed-particle-size assumption for limb observation retrievals (Bourassa et al., 2023; Remai et al., 2026).

The average SAOD in the tropics as well as the northern and southern extratropics agrees well between CMIP datasets, CREST, OMPS-LP, and SCIAMACHY (Fig. S11). However, the SAOD in CMIP7 is persistently lower (on average, 7% for CREST, 18% for OMPS-LP, and 21% for SCIAMACHY), which may be a result of the wavelength conversion to 550 nm and biases therein (Damadeo et al., 2024). Further, the seasonal cycle in the extratropics is more pronounced in CREST, OMPS-LP, and SCIAMACHY than in CMIP7. This is the case even in periods where CREST and CMIP7/GloSSAC only rely on SAGE II, indicating differences in observation processing, such as CREST's seasonal-cycle adjustment (Sofieva et al., 2024b).

https://doi.org/10.5194/egusphere-2026-4193
Preprint. Discussion started: 23 July 2026

3.2 Effective radius

The effective radius is the cross-sectional area-weighted mean radius of the particle size distribution. While typically not required by radiation code, it plays a key role in the CMIP7 stratospheric aerosol forcing as an intermediate result from which all other optical properties (except for the extinction at 525 nm) are derived. These derived properties include the aerosol single scattering albedo and asymmetry factor, which are inputs for commonly used radiative transfer models (e.g., Iacono et al., 2008). Note that the relationship of the effective radius to other properties depends on the assumed particle size distribution. CMIP7 uses a bimodal lognormal distribution with fixed geometric standard deviations for both modes (Aubry et al., 2026b).

3.2.1 Comparison of CMIP6 and CMIP7

The global-mean effective radius of ambient aerosol particles throughout the stratosphere is larger in CMIP7 at 0.132 μm compared to 0.118 μm in CMIP6 over the 1850–2014 period covered by both CMIP6 and CMIP7 (Fig. 14). In years without eruptions, the same holds as can also be seen in the baseline of the global mean (Fig. 14a). This larger effective radius in CMIP7 is mostly due to differences in the effective radius of non-volcanic background. For CMIP6, the non-volcanic background effective radius further shows a linear increase with time, while, in CMIP7, it remains constant during the pre-satellite era. For the CMIP6 data, this linear trend in background aerosols was introduced from 1850 to 1978 to represent rising anthropogenic emissions of tropospheric aerosols, some of which are transported into the stratosphere (Aubry et al., 2026b). During the satellite era, both CMIP6 and CMIP7 show more variation in the effective radius, also for volcanically quiescent years.

In contrast to CMIP6, small-magnitude eruptions show up in the effective radius data during the pre-satellite era in the CMIP7 dataset as a result of the inclusion of more small-magnitude eruptions (Fig. 14a). The timing of eruptions is often similar between the two datasets, while the magnitude and latitudinal extent of changes in the effective radius differ (Fig. 14a–c). The effective radius of aerosol particles tends to be smaller in CMIP6 during eruptions, especially in the pre-satellite era. For the CMIP7 effective radius data, effects of eruptions tend to appear in both hemispheres and across latitudes, while, in CMIP6, they are confined to one hemisphere more often, mirroring spatial structures in extinction (Fig. 14b, c).

Differences between the CMIP6 and CMIP7 datasets are most pronounced during the 1960s and 1970s. Throughout these decades, the CMIP6 effective radius is enhanced and variable, while, in CMIP7, the 1963 Mt. Agung eruption shows up as a sharp peak, with only one smaller eruption in the following years. That CMIP6 shows more variations in effective radius is likely due to the inclusion of stellar extinction measurements for the years 1961–1978 (Stothers, 2001), which include many small to moderate perturbations. The CMIP7 dataset, on the other hand, only shows eruptions that appeared in ice-core data. As a consequence of this difference in the underlying data, the 1963 Mt. Agung eruption also has a stronger signal in CMIP6 in the year following the eruption (Fig. S6). In CMIP6, the eruption appears strongest in the tropics, whereas CMIP7 shows slightly more of a mid- and high-latitude signal. Such differences between CMIP6 and CMIP7 in the effective radius signal associated with individual eruptions exist especially during the pre-satellite era. After the 1861 eruption, for example, the effective radius is larger for CMIP7 than CMIP6 (Fig. S4). The signal extends across the hemispheres and further up into the atmosphere in the CMIP7 effective radius data, whereas it is more focussed on the SH for CMIP6. Following the 1902 Santa María eruption,

https://doi.org/10.5194/egusphere-2026-4193
Preprint. Discussion started: 23 July 2026

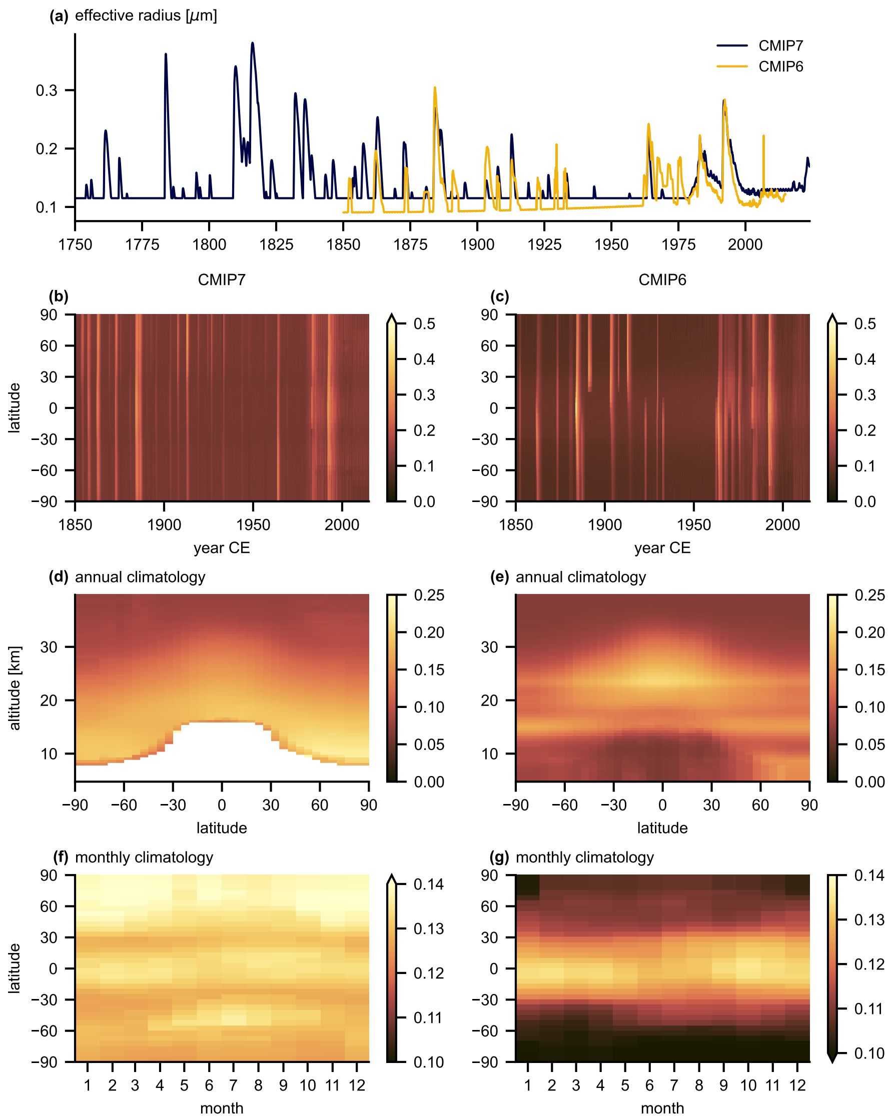

Figure 14. Effective aerosol radius in CMIP7 (a, b, d, f) and CMIP6 (a, c, e, g). (a) Global monthly-mean time series averaged along altitude in CMIP7 (blue) and CMIP6 (yellow). (b, c) Latitudinal change with time from 1850 to 2014 averaged along altitude. (d, e) Annual climatology, from 1850 to 2014 (CMIP6)/2021 (CMIP7). (f, g) Latitudinal change in climatologies with month. For the vertical integration of the latitudinal profiles the troposphere in CMIP6 was masked as in CMIP7.

CMIP6 effective radius shows a strong signal in the NH, which is almost completely absent from the CMIP7 data (Fig. S5). During the satellite era, the eruption signal is more alike, as shown by the similarities for the 1982 El Chichón and 1991 Mt. Pinatubo eruptions (Figs. S8, S9).

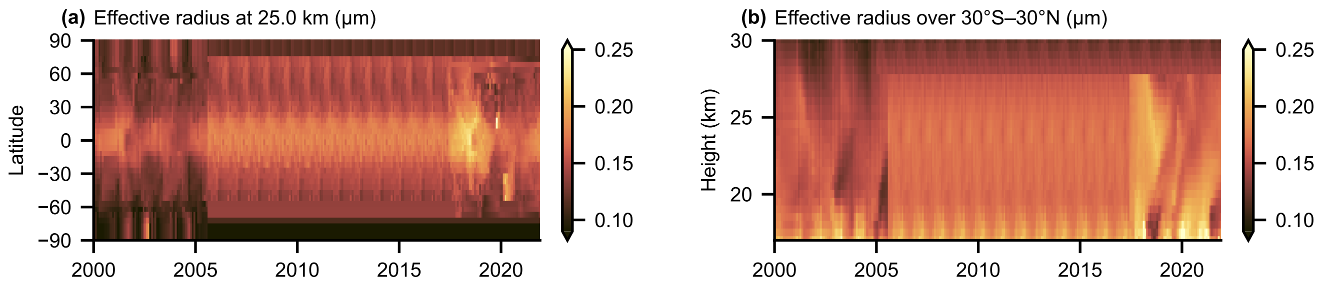

Figure 15. Effective radius in CMIP7 for 2000–2021, including the end of the SAGE II mission in August 2005. (a) Effective radius at an altitude of 25 km. (b) Effective radius averaged over 30°S–30°N.

For the climatological means, patterns across altitude and latitude are smoother for the CMIP7 annual mean than for CMIP6 (Fig. 14d, e). The patterns are dominated by the pre-satellite era, during which the difference between CMIP6 and CMIP7 is particularly pronounced and patterns are overall smoother than during the satellite era (Fig. S13). The CMIP6 data shows two pronounced bands of higher effective radius values around altitudes of 15 and 23 km that stretch across latitudes, seemingly an artefact of the methodology as they appear throughout the whole coverage period (Figs. 14d, e, S13).

Changes in the monthly climatologies are small in magnitude throughout the year, with overall higher values for CMIP7 (Fig. 14f, g). Both datasets show lower effective radius values in the SH compared to the NH, with particularly low values in high southern latitudes. The subtropics show particularly low values in effective radius in CMIP7, comparable with the SH high latitudes. In CMIP6, on the other hand, the effective radius in the tropics and subtropics is largest in the dataset.

3.2.2 Effective radius in the post-SAGE II period

GloSSAC, on which CMIP7 is based after 1979, aims to provide the extinction at 525 nm and 1020 nm based on multi-wavelength observations (Thomason et al., 2018; Kovilakam et al., 2020). The effective radius in CMIP7 is derived from the ratio of 525-to-1020-nm extinction; all other CMIP7 optical properties except for the extinction at 525 nm are then derived from the effective radius. However, during the gap between the SAGE II and SAGE III missions (September 2005–May 2017), GloSSAC relies on single-wavelength observations, so that the 1020-nm extinction is derived from a monthly, climatological empirical relationship (Kovilakam et al., 2020). The resulting effective radius in CMIP7 therefore has a repeating seasonal cycle over 2005–2017 but no other variability (Fig. 15). In addition to the climatological values, there are discontinuities at an altitude of around 28 km and poleward of 75°N/S that persist after the SAGE III data become available in 2017.

3.2.3 Comparison with SCIAMACHY retrievals

The effective radius based on SCIAMACHY observations, calculated from the retrieved particle size distribution, enables independent validation. SCIAMACHY and SAGE II observations overlap from 2002 to 2005. The zonal-mean effective radius at heights of 18.4 km and 25.0 km during this period is shown in Figure 16. At both altitudes, CMIP7 and SCIAMACHY agree

https://doi.org/10.5194/egusphere-2026-4193
Preprint. Discussion started: 23 July 2026

on a mean effective radius of 0.13 μm to 0.15 μm, but CMIP7 appears biased high compared to SCIAMACHY in the tropics at 18.4 km. A high bias in the effective radius derived from SAGE II observations, which are included in GloSSAC, particularly at lower altitudes, has been noted before by Pohl et al. (2024). The effective radius from SCIAMACHY, in contrast, agrees with in situ optical particle counter measurements in mean value and time variations (Pohl et al., 2024), and shows strong consistency with nudged atmosphere–aerosol simulations for a case study of the 2009 Sarychev eruption (Pohl et al., 2026). The correlation of zonal means between CMIP7 and SCIAMACHY is weak. This may be attributed to the absence of large-magnitude eruptions, sparse observational sampling in GloSSAC, or differences in assumptions used to obtain particle sizes. CMIP7 assumes a bimodal lognormal particle size distribution with fixed geometric standard deviations, while Pohl et al. (2024) assume a unimodal distribution with a fixed number density profile.

An increase in effective radius at 18.4 km after volcanic eruptions is seen in both CMIP7 and SCIAMACHY, although magnitude and timing differ slightly (Fig. 16). The 2004/2005 Manam eruption is the largest during the shown period, exhibiting a different behaviour between CMIP7 and SCIAMACHY compared to the pre-Manam period. Pohl et al. (2026) found that the distribution of the effective radius from SCIAMACHY after Manam is roughly correct, but the assumed number density profile based on background conditions (Pohl et al., 2024) may account for altitude-dependent discrepancies with SAGE II, the product mainly used by CMIP7 during this period.

3.3 Volume and number density

The volume and number density of aerosol particles are included in the CMIP6 and CMIP7 forcing datasets as variables that are especially relevant for cloud and microphysical processes, as aerosols for example act as cloud condensation nuclei. The CMIP6 and CMIP7 global-mean time series of volume and number density are similar after 1880 and differ mostly in the small-magnitude eruptions present in CMIP7 discussed previously (Fig. 17a, b). Between 1850 and 1880, the CMIP7 data includes more eruptions. Eruptions that are present in both datasets during that period have larger magnitude in CMIP7 due to the additional improved reconstructions available for the CMIP7 dataset. Across latitudes, the CMIP7 number and volume density show stronger and more eruptions, especially in the NH high latitudes (Fig. S10). The latitude–altitude profiles during volcanically quiescent years of both number and volume density differ a little between CMIP6 and CMIP7, for example with a decreased number density in the tropical low stratosphere (Figs. 17, S15, S16).

In general, eruptions are more similar between the CMIP6 and CMIP7 datasets during the satellite era compared to the pre-satellite era, as can be seen in the similarities for the El Chichón (1982, Fig. S8) and Mt. Pinatubo (1991, Fig. S9) eruptions. This is because the versions of GloSSAC used in CMIP6 and CMIP7 are relatively similar. In the pre-satellite era, eruptions in the CMIP6 and CMIP7 datasets show more differences, which are specific to individual eruptions, but have in common that the eruption signals tend to be more localised in the CMIP6 variables (Figs. S4–S6). The 1861 eruption shows an overall stronger signal that extends further up into the atmosphere in CMIP7 in number and volume density (Fig. S4). The eruption signal is further much stronger in the NH for the CMIP7 variables, while it is mostly confined to the SH for CMIP6. Opposite to the 1861 eruption, the 1902 Santa María, and the 1963 Agung eruptions are overall stronger in CMIP6 (Figs. S5, S6). The

https://doi.org/10.5194/egusphere-2026-4193
Preprint. Discussion started: 23 July 2026

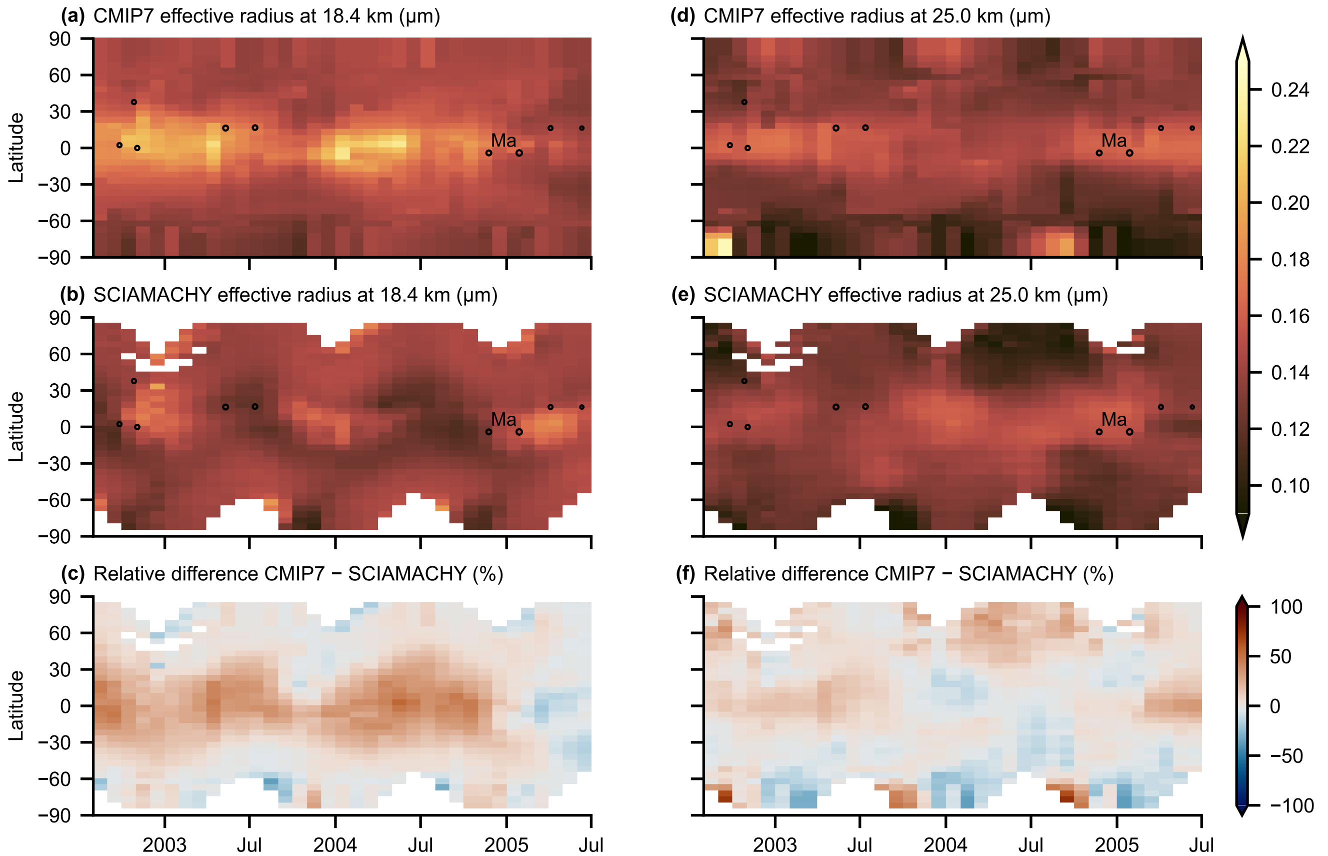

Figure 16. Effective aerosol radius in CMIP7 and SCIAMACHY satellite retrievals during the SAGE II overlap period (August 2002–July 2005). Data are in 3.3-km vertical bins, centred on altitudes of 18.4 km and 25.0 km. The Manam (Ma) eruption in late 2004 and early 2005 is mentioned in the text. Black circles indicate volcanic eruptions exceeding 0.05 Tg SO_2, scaled by injected SO_2 mass.

Santa María eruption is almost completely missing in CMIP7 (Fig. S5). The Agung eruption shows a more spread-out signal, strongest at SH high latitudes in CMIP7 that is more confined to southern tropical latitudes in CMIP6 (Fig. S6).

For both number and volume density, the annual climatologies show larger values in the CMIP7 dataset across latitudes and altitude (Fig. 17c–f). The CMIP7 number and volume density remain similar over the months with a strong latitudinal pattern and the strongest signal in the northern high latitudes (Fig. S10). The CMIP6 data, on the other hand, varies a little more with the time of year.

https://doi.org/10.5194/egusphere-2026-4193
Preprint. Discussion started: 23 July 2026

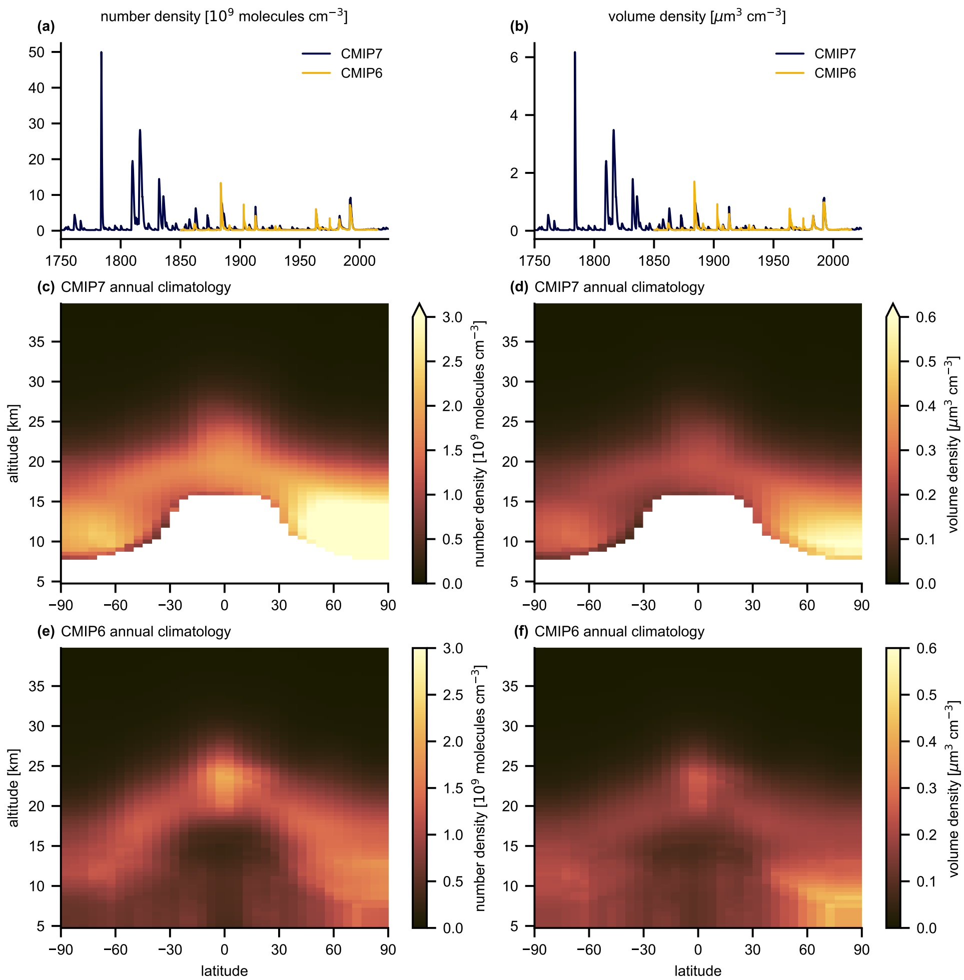

Figure 17. Number (left column) and volume density (right column) in CMIP7 (a, b, c, d) and CMIP6 (a, b, e, f). (a, b) Global monthly-mean time series averaged along altitude in CMIP7 (blue) and CMIP6 (yellow). (c, d, e, f) Annual climatology, from 1850 to 2014 (CMIP6)/2021 (CMIP7). For the vertical integration of the latitudinal profiles the troposphere in CMIP6 was masked as in CMIP7.

4 Discussion

4.1 SAOD underestimation following major eruptions

Our analysis showed that CMIP7 likely underestimates SAOD following the 1902 Santa María, 1921 Puyehue, 1928 Paluweh, 1929 Komagatake, 1963 Agung, and 1974 Fuego eruptions as compared to independent observations (Fig. 2). The 1921 Puyehue and 1928 Paluweh eruptions, which are identified by Stothers (1996), are not represented in the CMIP7 volcanic sulfur emission inventory. Among the eruptions examined, the 1902 Santa María and 1974 Fuego eruptions show significant dis-

https://doi.org/10.5194/egusphere-2026-4193
Preprint. Discussion started: 23 July 2026

crepancies in SAOD between CMIP7, CMIP6, and independent observations (Sect. 3.1.5). The year 1902 had three tropical eruptions: Santa María, Soufrière St. Vincent, and Pelée. In CMIP7, the 1902 Santa María eruption (VEI 6) is assigned 2 Tg SO_2 based on ice-core sulfate emissions from Sigl et al. (2015). The VEI 4 eruptions (e.g., the 1902 Soufrière St. Vincent and Pelée eruptions, the 1929 Komagatake eruption, and the 1974 Fuego eruption) are each assigned 0.08 Tg SO_2. However, an alternative volcanic SO_2 emission inventory, VolcanEESM (Neely III and Schmidt, 2016), suggests substantially higher values for these eruptions (see Fig. 9 in Aubry et al. (2026a) for the comparison between CMIP7 emissions and other volcanic sulfur emission inventories). VolcanEESM assigns emissions of 0.2 Tg SO_2 and 2.3 Tg SO_2 for Soufrière St. Vincent and Pelée, respectively, using estimation from Stothers (1996), and 3.8 Tg SO_2 for Santa María using the ice-core inventory from Gao et al. (2008), totalling 6.3 Tg SO_2 for the three 1902 eruptions, which is approximately three times the CMIP7 estimate. Similarly, the 1929 Komagatake eruption and the 1974 Fuego eruption are assigned as 2 and 3 Tg SO_2 in VolcanEESM (Bauer, 1979; Stothers, 1996) respectively, which is nearly 25–40 times larger than the CMIP7 estimate of 0.08 Tg SO_2 for a VEI 4 eruption. Observed SAOD magnitudes from pyrheliometric measurements, stellar extinction, and lunar eclipses substantially exceed CMIP7 simulations for years following the 1902 and 1974 eruptions (Figs. 7, 9). This suggests that CMIP7 likely underestimates volcanic SO_2 emissions for these years, potentially due to uncertainties in the ice-core-derived estimates for the 1902 Santa María eruption, the assumption of 0.08 Tg SO_2 assignment for VEI 4 eruptions from the GVP database, or a combination of both. Anthropogenic sulfate pollution in Greenland ice cores after 1900 introduces substantial uncertainties in the isolation of volcanic sulfate signals (Toohey and Sigl, 2017). In addition, satellite records show that VEI 4 eruptions can produce volcanic stratospheric sulfur injections spanning multiple orders of magnitude between 0 and 2 Tg SO_2 (Schindlbeck-Belo et al., 2024). For the 1861 unidentified eruption attributed to Mt. Kie Besi, a VEI 4 eruption, a value of 9 Tg SO_2 is assigned based on ice-core records. Using a fixed value of 0.08 Tg SO_2 for VEI 4 eruptions in CMIP7 may under- or overestimate individual eruptions (Aubry et al., 2026a).

During the satellite period, where optical properties are derived from direct satellite observations instead of volcanic emission estimates, the SAOD differences between CMIP6 and CMIP7 arise only from updates in GloSSAC data versions. However, gaps between satellite observations create challenges in accurately capturing aerosol extinction following major eruptions, including the 1982 El Chichón and the 1991 Mt. Pinatubo eruptions (Figs. 10, 11).

Our analysis shows that both CMIP6 and CMIP7 likely underestimate the peak SAOD following the 1982 El Chichón eruption as a result of a lack of good alternative measurements to fill the satellite data gap (Fig. 10, Sect. 3.1.5). Lidar observations from Mauna Loa suggest a peak SAOD at 550 nm of up to 0.4 in the tropics (20°N) within three months following the eruption, while CMIP6 and CMIP7 have an SAOD at 550 nm of around 0.05 and a discontinuous zonal structure (Fig. 10c). For the 1991 Mt. Pinatubo eruption, our comparison shows excellent agreement between CMIP6, CMIP7 and other satellite datasets, although lidar data indicate an extinction peaking at around 0.3 rather than 0.1, which may be reasonably explained by uncertainties in conversion factors used for the lidar data (Fig. 11). The SAOD magnitude and timescale simulated with EVA_H, albeit calibrated on GloSSAC over 1979–2015, agree with the satellite datasets for the 1982 El Chichón and 1991 Mt. Pinatubo eruptions (Figs. 10, 11). This provides confidence to derive pre-satellite aerosol optical properties from emis-

https://doi.org/10.5194/egusphere-2026-4193
Preprint. Discussion started: 23 July 2026

sions. The EVA_H-simulated SAOD is smoother in space and time, and exhibits greater hemispheric symmetry, owing to the idealised model structure (Aubry et al., 2020).

The underestimation of SAOD following major eruptions would affect the CMIP7 historical simulations regardless of whether they use volcanic sulfur emissions or prescribed stratospheric aerosol optical properties. The potential implications of such underestimation are discussed in Section 4.3 below.

4.2 Limitations of satellite-era observations

While the optical properties in CMIP7 are likely more realistic during the satellite period than the pre-satellite period, new issues arise with the use of satellite observations. First, there are observational gaps during major eruptions (1982 El Chichón and 1991 Mt. Pinatubo) that need to be filled with alternative measurements, such as ground-based lidars, or empirical functions. This can lead to unrealistic spatial structures due to the spatial extrapolation of point measurements (e.g., Fig. 10c), even though care is taken in GloSSAC to create a homogeneous dataset.

Secondly, only single-wavelength data are available during the post-SAGE II period (2005–2017) so that optical properties need to be derived from climatological empirical relationships rather than observed data. This introduces discontinuities in properties other than the 525-nm extinction (Fig. 15). Integrating SCIAMACHY and OMPS-LP observations into future GloSSAC versions may alleviate this issue (Kovilakam et al., 2020, 2025).

Thirdly, even during well-observed periods, any single satellite dataset does not provide a perfect ground truth. There can be large differences between instruments and even retrievals from the same instrument (e.g., Kovilakam et al., 2025; Bourassa et al., 2023), particularly for the vertical structure of optical properties following volcanic eruptions. These differences stem, for example, from the satellite viewing geometry (which changes the instrumental sensitivity by location), sampling coverage (limb scattering observations allow better sampling than solar occultation observations, for example, the 2022 Hunga Tonga–Hunga Ha'apai eruption is delayed by a month in GloSSAC compared to OMPS-LP; Fig. 13), and retrieval assumptions on the particle size. Thus, there may be a benefit in using different retrievals in addition to different instruments in multi-instrument records like GloSSAC and CREST. Combining observations from different instruments necessitates wavelength interpolation, however, which may introduce biases unless corrected (Damadeo et al., 2024).

Finally, even during periods where multi-wavelength observations are available, the optical properties derived in CMIP7 using Mie scattering theory may not be accurate. For example, the effective radius over 2002–2005 in CMIP7 and as retrieved from SCIAMACHY bear little resemblance (Fig. 16), which could be a result of differing assumptions about the particle size distribution, such as the number of modes and the geometric standard deviation.

4.3 Implications for CMIP7 historical simulations

The underestimation of the SAOD from major eruptions has important implications for CMIP7 historical simulations. As discussed above, these biases stem from underestimated volcanic SO_2 emissions in pre-satellite eruptions (1902 Santa María/Pelée and 1974 Fuego eruptions), observational gaps in satellite instruments (1982 El Chichón eruption), and eruptions missing in CMIP7 despite evidence in independent observations (1921 Puyehue, 1928 Paluweh, and 1929 Komagatake eruptions).

https://doi.org/10.5194/egusphere-2026-4193
Preprint. Discussion started: 23 July 2026

These issues have direct impacts on radiative forcing and historical temperatures. The peak global monthly-mean stratospheric aerosol radiative forcing following the 1902 eruptions (Soufrière St. Vincent, Pelée, Santa María) is 1.2 W m^{-2} weaker in CMIP7 compared to CMIP6, and 0.8 W m^{-2} weaker following the 1974 Fuego eruption (Aubry et al., 2026b). Simulations using a simple climate model indicate that these differences in radiative forcing correspond to approximately 0.1°C higher global annual-mean surface air temperature in CMIP7 during the first two post-eruption years (Fig. 12 in Aubry et al., 2026b). On longer timescales, the 1900–1980 global-mean surface temperature in the simple climate model simulation is 0.015°C higher using CMIP7 volcanic forcing compared to when using CMIP6 forcing, suggesting a potential warm bias related to these eruptions. Full-complexity climate models using CMIP7 stratospheric aerosol forcing would likely simulate a similar warm bias in the historical period.

In addition to aerosol extinction, other volcanic aerosol properties, such as effective radius, surface area density, and number density, are likely also underestimated following the 1902 and 1974 eruptions (Figs. S5, S7). Since these aerosol properties affect stratospheric chemistry and radiative processes, their underestimation may consequently introduce biases in the simulated response in ozone following these eruptions and thus the CMIP7 historical ozone forcing, which is partially derived from volcanic forcing.

Given the large differences in CMIP6 and CMIP7 stratospheric aerosol forcing datasets, a multi-model intercomparison study between the CMIP7 Assessment Fast Track and CMIP6 historical simulations for major eruptions in the historical period would be valuable for quantifying how these revised stratospheric aerosol forcing estimates affect the simulated climate response, and for reducing uncertainty in historical temperature and ozone reconstructions. These discrepancies highlight the importance of independent observational constraints on volcanic forcing.

4.4 Future directions for improvement

4.4.1 Improved constraints on volcanic SO_2 emission

To improve future forcing datasets, pyrheliometric measurements, lunar eclipse data, stellar extinction data, and ground-based lidar measurements can be used to provide constraints on volcanic SO_2 emission inventories, particularly for eruptions in the pre-satellite era with a lack of confidence in the volcanic SO_2 emissions, and for satellite-era eruptions with observational gaps. Current pre-satellite volcanic sulfur emission estimates rely heavily on ice-core sulfate records, which have substantial uncertainties related to volcanic sulfate deposition and aerosol transport processes. Additionally, the CMIP7 approach of assigning uniform emissions based on VEI for small-to-moderate magnitude eruptions (i.e., 0.08 Tg SO_2 for VEI 4 eruptions and 2.78 Tg SO_2 for VEI 5 eruptions) does not capture the considerable variability in actual emissions within each VEI category (Schindlbeck-Belo et al., 2024; Aubry et al., 2026a). Such uncertainties of different volcanic sulfur emission inventories could be sampled using forcing ensembles with stochastic eruption parameters in simple climate models like FaIR (Leach et al., 2021; Lücke et al., 2023; Verkerk et al., 2025).

Independent observational constraints on SAOD and alternative volcanic emission inventories can help address these existing limitations by providing complementary measurements. Recent efforts to digitise and compile stellar extinction data from

https://doi.org/10.5194/egusphere-2026-4193
Preprint. Discussion started: 23 July 2026

observatories worldwide (Rodgers, 2022; Rodgers and Toohey, 2026), systematic analysis of lunar eclipse observations (Boissel and Guillet, 2026), and data rescue activities by the APARC project to recover historical lidar data (Antuña-Marrero et al., 2020c, 2021, 2023) make such data more accessible for volcanic forcing reconstruction. Future work should systematically incorporate these observational datasets to improve volcanic SO_2 estimates for poorly constrained eruptions and reduce uncertainties in historical volcanic forcing.

4.4.2 Improvement in non-volcanic background aerosols

In addition to refining volcanic emission estimates, future forcing datasets should also improve the representation of non-volcanic stratospheric background aerosols. Both CMIP6 and CMIP7 aerosol extinction used a similar methodology in deriving non-volcanic stratospheric background aerosols in the pre-satellite period (Luo, 2018; Aubry et al., 2026b). Based on the stratospheric sulfur burden simulated using SOCOL-AERv1 in Sheng et al. (2015), the climatological mean of a volcanically quiescent satellite period is scaled with an increasing trend between 1850 (0.074 Tg S) and 2000 (0.11 Tg S) using the total background stratospheric sulfur burden. Our results show that the amplitude of seasonal cycles is substantially greater in CMIP7 than in CMIP6 (Fig. S3). Additionally, the trend of SAOD from non-volcanic stratospheric background aerosols is linear in CMIP7 and non-linear in CMIP6. A recent study revisited the global sulfur budget in volcanically quiescent periods using nine global circulation models, showing that the multi-model mean stratospheric aerosol burden is 0.156 ± 0.051 Tg S, compared to 0.163 Tg S derived from the SAGE-3λ observational dataset (Brodowsky et al., 2024), both of which are larger than the values used in scaling the non-volcanic background aerosols in CMIP6/7. The treatment of non-volcanic stratospheric background aerosols, including their scaling and seasonal cycles, should be improved in future forcing datasets, e.g. by using historical interactive stratospheric aerosol model simulations with no volcanic emissions (Yu et al., 2016; Aubry et al., 2026b).

4.4.3 Inclusion of other stratospheric constituents

Beyond background aerosol representation, the CMIP7 stratospheric aerosol optical properties and emission datasets both consider mainly stratospheric volcanic sulfur, except during the satellite period when the optical properties dataset uses GloSSAC observations that represent total stratospheric aerosol load. Some emissions and sources of stratospheric aerosols are omitted in CMIP7, including (1) non-volcanic emissions in the satellite era such as pyrocumulonimbus (pyroCb) injections (Damany-Pearce et al., 2022), spacecraft emissions (Murphy et al., 2023), and meteoric dust particles (Schneider et al., 2021); (2) tropospheric–stratospheric transport of aerosols; and (3) other volcanic emissions such as halogens and water vapour (Theys et al., 2014; Carn et al., 2016; Khaykin et al., 2022). In the CMIP7 volcanic SO_2 emission dataset, the pyroCb injections from wildfire events are not included, highlighting the need for a more systematic treatment of stratospheric wildfire aerosols. The recent development of a global pyroCb emission inventory provides information on the injection altitude and mass of smoke particles from pyroCb events during 2013–2023 (Peterson et al., 2025). In addition to wildfire aerosols, recent satellite measurement studies provide data on volcanic halogen and water vapour emissions and their injection altitudes (Theys et al., 2014; Carn et al., 2016; Khaykin et al., 2022). Incorporating these additional sources and species would further improve future stratospheric aerosol forcing datasets.

https://doi.org/10.5194/egusphere-2026-4193
Preprint. Discussion started: 23 July 2026

5 Conclusions

This study presents Part 3 of the documentation of the stratospheric aerosol forcing datasets for CMIP7. We compare CMIP6 and CMIP7 stratospheric aerosol optical properties, and evaluate them against an extensive compilation of observational records including pyrheliometric measurements, stellar extinction observations, lunar eclipse data, lidar retrievals, and satellite data from SCIAMACHY, OMPS-LP, and CREST. These include pre-satellite era records on which CMIP6 depends (lunar eclipses for the 1850–1881 period, pyrheliometer, stellar extinction), as well as datasets not used in CMIP6 (lunar eclipses, lidar retrievals). CMIP7 adopts a different, emission-based approach from CMIP6, converting volcanic SO_2 emissions to stratospheric aerosol optical properties using the EVA_H model for pre-satellite era eruptions, an approach consistent with VolMIP and PMIP.

Our results show that the peak SAOD of most large-magnitude eruptions, including Krakatau (1883), Katmai (1912), Agung (1963), El Chichón (1982), and Pinatubo (1991), agree reasonably well (within 20% difference in peak SAOD values) between CMIP6 and CMIP7. CMIP7 incorporates more small-to-moderate magnitude eruptions in the pre-satellite era previously absent from CMIP6, an addition supported by lunar eclipse data (Fig. 2). As a result, there are numerous years in CMIP7 with greater SAOD perturbations than CMIP6. Comparison of satellite versus pre-satellite era datasets suggests a lack of small-magnitude eruptions in the pre-satellite era, but that SO_2 emissions and SAOD are likely overestimated for moderate-magnitude eruptions overall (Aubry et al., 2026a). However, our comparison to observational datasets suggests that CMIP7 likely underestimates the SAOD of several moderate-magnitude eruptions that are captured in CMIP6. For instance, pyrheliometric measurements from Stothers (1996) indicated SAOD perturbations from Puyehue (1921) and Paluweh (1928); yet these eruptions are not included in CMIP7 because they are not detected in ice cores and have a VEI < 4. Volcanic SO_2 emissions and SAOD for moderate-magnitude eruptions including Soufrière St. Vincent, Pelée, Santa María (1902), Komagatake (1929), and Fuego (1974), are likely underestimated in CMIP7 because they are not detected in ice cores. In addition, we find that the SAOD after the 1982 El Chichón eruption is likely underestimated in both CMIP6 and CMIP7, according to lidar and stellar extinction measurements, as a result of observational gaps in satellite instruments in GloSSAC data.

Additional sources of uncertainty in the CMIP7 dataset include spatial discontinuities in satellite measurements due to data gaps, the representation of non-volcanic background aerosols in the pre-satellite period, and the lack of other stratospheric species in the pre-satellite CMIP7 volcanic sulfur emission inventory. Our evaluation reveals the potential SAOD underestimations in both CMIP6 and CMIP7 for eruptions in the pre-satellite period, highlighting that the historical stratospheric aerosol record remains highly uncertain.

These findings point to several opportunities for future improvement of stratospheric aerosol forcing datasets. Combining CMIP6's use of observational constraints to adjust emissions with CMIP7's more extensive emission inventory, which better captures eruptions of all magnitudes, can provide a valuable basis for constraining historical volcanic SO_2 emissions. Continuous improvements in stratospheric aerosol proxy records (e.g., lunar eclipses and stellar extinction data), alongside ongoing data rescue activities coordinated by the APARC (Antuña-Marrero et al., 2020c, 2021, 2023), will further enhance our understanding of historical stratospheric aerosol forcing. Given the large differences in forcing between CMIP6 and CMIP7, climate model responses to these revised stratospheric aerosol forcing estimates should be assessed in historical simulations.

Code and data availability. The code to reproduce this paper is available for peer review on Zenodo under https://zenodo.org/records/21385639?preview=1&token=eyJhbGciOiJIUzUxMiJ9.eyJpZCI6IjhlNjAxODg4LTNhYTgtNDA3MS04NThmLWY0M2Y0YWQ4MWUwZiIsImRhdGEiOnt9LCJyYW5kb20iOiJhZjE3MmIzNzNlNDc2Njc5ZjBmZDc0MmZlY2I5NDZiMiJ9.xrQ-dfoB0EmJtPkJk90xxCQr95QXtgcUtVEE0ipl3TvlA4XxXRZgTH9hR4i4NCHtO-bEx5F9W2yTU6_0od_gFA (Chim et al., 2026); the record will be published upon acceptance. CMIP7 and CMIP6 stratospheric aerosol forcing data are available on ESGF under https://doi.org/10.25981/ESGF.input4MIPs.CMIP7/2522673 (Aubry, 2025) and https://doi.org/10.22033/ESGF/input4MIPs.1681 (ETH Zürich, 2017), respectively. Lunar eclipse data are available on Zenodo under https://doi.org/10.5281/zenodo.18461205 (Boissel and Guillet, 2026). Pyrheliometer data are extracted from figures and tables in Stothers (1996). Stellar extinction data are available on Zenodo under https://doi.org/10.5281/zenodo.18488959 (Rodgers and Toohey, 2026). SCIAMACHY and OMPS-LP data are available upon request via https://www.iup.uni-bremen.de/DataRequest/ (Rozanov, 2026). CREST data are available on FMI's research data repository under https://doi.org/10.57707/fmi-b2share.dfe14351fd8548bcaca3c2956b17f665 (Sofieva et al., 2024a). Lidar data are available on PANGAEA under https://doi.org/10.1594/PANGAEA.912770 (Antuña-Marrero et al., 2020c) and https://doi.org/10.1594/PANGAEA.922105 (Antuña-Marrero et al., 2020a), and through personal communication from John E. Barnes (Mauna Loa), Sergey M. Khaykin (Haute-Provence), and Thierry Leblanc (Table Mountain). Searchlight data are available on PANGAEA under https://doi.org/10.1594/PANGAEA.949377 (Antuña-Marrero et al., 2023). EVA_H simulations during the satellite period are available upon request from Thomas J. Aubry.

Author contributions. MMC, DS, and EZ share first authorship with equal contributions, and the ordering among the three is interchangeable. MMC, DS, and EZ conceptualised the study and performed the data analysis and visualisation with advice from TJA. LB and SG provided expert guidance on the lunar eclipses data, BR and MT on the stellar extinction data. CP provided the SCIAMACHY data, AR provided OMPS-LP data, and TJA provided EVA_H simulations used in this study. MMC, DS, and EZ wrote the first draft of the manuscript. TJA and MT contributed to the description of CMIP6 and CMIP7 stratospheric aerosol forcing, LB and SG contributed to the description of lunar eclipse data, BR contributed to the description of stellar extinction data. All the co-authors reviewed and provided feedback on the analysis and manuscript.

Competing interests. The authors declare that they have no competing interests.

Acknowledgements. We warmly thank the numerous people who commented on the datasets at workshops, meetings, and on input4MIPs GitHub, and whose feedback helped with writing this evaluation paper. We thank Juan Carlos Antuña Marrero for his advice on lidar data.

MMC acknowledges funding support from the Croucher Foundation via a Croucher Postdoctoral Fellowship. DS acknowledges support by the National Science Foundation under Award No. 2202526. EZ acknowledges funding through the Federal Ministry of Education and

Research of Germany (PalMod III, grant no. 01LP2310A). MT and BR acknowledge support from the Alliance Program of the Natural Sciences and Engineering Research Council of Canada through grant ALLRP 597559-24, and from the Canadian Space Agency through contribution 24SUHAWCSD. TJA acknowledges support from the European Space Agency "Volcanic forcing for CMIP" project of the Climate Change Initiative (CCI) (ESA Contract No. 4000145911/24/I-LR). CP acknowledges support from Svenska Forskningsrådet Formas (grant no. 2020-00997), the Swedish National Space Agency (grant no. 2025-00200), and the Deutsche Forschungsgemeinschaft (Research Unit VolImpact grant no. 398006378). The development and processing of SCIAMACHY, OMPS-LP, and CREST datasets at the University of Bremen was funded in part by the European Space Agency (ESA) via the CREST project, by the German Research Foundation (DFG) via the research unit VolImpact (grant no. FOR2820), and by the University of Bremen and state of Bremen. We gratefully acknowledge the computing time granted by the Resource Allocation Board and provided for the supercomputers Lise and Emmy at NHR@ZIB and NHR@Göttingen as part of the NHR infrastructure. The processing of OMPS-LP dataset used in this study, as well as some datasets included in the CREST climate data record, was conducted using computing resources under project no. hbk00098. The SCIAMACHY data used in this study were processed using the HPC facilities of the IUP, University of Bremen, funded by DFG/FUGG grant nos. INST 144/379-1 and INST 144/493-1.

https://doi.org/10.5194/egusphere-2026-4193
Preprint. Discussion started: 23 July 2026

References

Ammann, C. M., Meehl, G. A., Washington, W. M., and Zender, C. S.: A monthly and latitudinally varying volcanic forcing dataset in simulations of 20th century climate, Geophysical Research Letters, 30, 2003GL016 875, https://doi.org/10.1029/2003GL016875, 2003.

Antuña-Marrero, J. C., Mann, G. W., Barnes, J., Rodríguez-Vega, A., Shallcross, S., Dhomse, S., Fiocco, G., and Grams, G. W.: The first ever multi-year lidar dataset of the stratospheric aerosol layer, from Lexington, MA, and Fairbanks, AK, January 1964 to July 1965, https://doi.org/10.1594/PANGAEA.922105, 2020a.

Antuña-Marrero, J.-C., Mann, G. W., Keckhut, P., Avdyushin, S., Nardi, B., and Thomason, L. W.: Shipborne lidar measurements showing the progression of the tropical reservoir of volcanic aerosol after the June 1991 Pinatubo eruption, Earth System Science Data, 12, 2843–2851, https://doi.org/10.5194/essd-12-2843-2020, 2020b.

Antuña-Marrero, J. C., Mann, G. W., Keckhut, P., Avdyushin, S. I., Nardi, B., and Thomason, L. W.: Ship borne lidar measurements in the Atlantic of the 1991 Mt Pinatubo aerosol cloud, https://doi.org/10.1594/PANGAEA.912770, 2020c.

Antuña-Marrero, J.-C., Mann, G. W., Barnes, J., Rodríguez-Vega, A., Shallcross, S., Dhomse, S. S., Fiocco, G., and Grams, G. W.: Recovery of the first ever multi-year lidar dataset of the stratospheric aerosol layer, from Lexington, MA, and Fairbanks, AK, January 1964 to July 1965, Earth System Science Data, 13, 4407–4423, https://doi.org/10.5194/essd-13-4407-2021, 2021.

Antuña-Marrero, J. C., Mann, G. W., Barnes, J., Calle, A., Dhomse, S., Cachorro Revilla, V. E., Deshler, T., Zhengyao, L., Sharma, N., and Elterman, L.: Tropospheric and stratospheric aerosol extinction and stratospheric aerosol optical depth from searchlight measurements conducted at White Sands, New Mexico, US between December 1963 and December 1964, https://doi.org/10.1594/PANGAEA.949377, 2023.

Antuña-Marrero, J.-C., Mann, G. W., Barnes, J., Calle, A., Dhomse, S. S., Cachorro, V. E., Deshler, T., Li, Z., Sharma, N., and Elterman, L.: The Recovery and Re-Calibration of a 13-Month Aerosol Extinction Profiles Dataset from Searchlight Observations from New Mexico, after the 1963 Agung Eruption, Atmosphere, 15, 635, https://doi.org/10.3390/atmos15060635, 2024.

Arfeuille, F., Weisenstein, D., Mack, H., Rozanov, E., Peter, T., and Brönnimann, S.: Volcanic forcing for climate modeling: a new microphysics-based data set covering years 1600–present, Climate of the Past, 10, 359–375, https://doi.org/10.5194/cp-10-359-2014, 2014.

Aubry, T.: input4MIPs.CMIP7.uoexeter.UOEXETER-CMIP-2-2-1, https://doi.org/10.25981/ESGF.INPUT4MIPS.CMIP7/2522673, 2025.

Aubry, T. J., Toohey, M., Marshall, L., Schmidt, A., and Jellinek, A. M.: A New Volcanic Stratospheric Sulfate Aerosol Forcing Emulator (EVA_H): Comparison With Interactive Stratospheric Aerosol Models, Journal of Geophysical Research: Atmospheres, 125, e2019JD031 303, https://doi.org/10.1029/2019JD031303, 2020.

Aubry, T. J., Sigl, M., Toohey, M., Chim, M. M., Verkerk, M., Schmidt, A., and Carn, S. A.: Stratospheric aerosol forcing for CMIP7 (part 2): Volcanic sulfur dioxide emissions, https://doi.org/10.5194/egusphere-2026-546, 2026a.

Aubry, T. J., Toohey, M., Khanal, S., Chim, M. M., Verkerk, M., Johnson, B., Schmidt, A., Kovilakam, M., Sigl, M., Nicholls, Z., Thomason, L., Naik, V., Rieger, L., Stiller, D., Ziegler, E., Durack, P., and Smith, I. H.: Stratospheric aerosol forcing for CMIP7 – Part 1: optical properties for pre-industrial, historical, and scenario simulations, Geoscientific Model Development, 19, 3725–3756, https://doi.org/10.5194/gmd-19-3725-2026, 2026b.

Avdyushin, S. I., Tulinov, G. F., Ivanov, M. S., Kuzmenko, B. N., Mezhuev, I. R., Nardi, B., Hauchecorne, A., and Chanin, M. L.: 1. Spatial and temporal evolution of the optical thickness of the Pinatubo aerosol cloud in the northern hemisphere from a network of ship-borne and stationary lidars, Geophysical Research Letters, 20, 1963–1966, https://doi.org/10.1029/93GL00485, 1993.

https://doi.org/10.5194/egusphere-2026-4193
Preprint. Discussion started: 23 July 2026

Barnes, J. E. and Hofmann, D. J.: Lidar measurements of stratospheric aerosol over Mauna Loa Observatory, Geophysical Research Letters, 24, 1923–1926, https://doi.org/10.1029/97GL01943, 1997.

Bauer, E.: A catalog of perturbing influences on stratospheric ozone, 1955–1975, Journal of Geophysical Research: Oceans, 84, 6929–6940, https://doi.org/10.1029/JC084iC11p06929, 1979.

Boissel, L. and Guillet, S.: Lunar eclipse luminosity and derived stratospheric aerosol optical depth (SAOD), 1750–2022, https://doi.org/10.5281/zenodo.18461205, 2026.

Bourassa, A. E., Zawada, D. J., Rieger, L. A., Warnock, T. W., Toohey, M., and Degenstein, D. A.: Tomographic Retrievals of Hunga Tonga-Hunga Ha'apai Volcanic Aerosol, Geophysical Research Letters, 50, e2022GL101 978, https://doi.org/10.1029/2022GL101978, 2023.

Brodowsky, C. V., Sukhodolov, T., Chiodo, G., Aquila, V., Bekki, S., Dhomse, S. S., Höpfner, M., Laakso, A., Mann, G. W., Niemeier, U., Pitari, G., Quaglia, I., Rozanov, E., Schmidt, A., Sekiya, T., Tilmes, S., Timmreck, C., Vattioni, S., Visioni, D., Yu, P., Zhu, Y., and Peter, T.: Analysis of the global atmospheric background sulfur budget in a multi-model framework, Atmospheric Chemistry and Physics, 24, 5513–5548, https://doi.org/10.5194/acp-24-5513-2024, 2024.

Carn, S.: Multi-Satellite Volcanic Sulfur Dioxide L4 Long-Term Global Database V4, https://doi.org/10.5067/MEASURES/SO2/DATA405, 2024.

Carn, S., Clarisse, L., and Prata, A.: Multi-decadal satellite measurements of global volcanic degassing, Journal of Volcanology and Geothermal Research, 311, 99–134, https://doi.org/10.1016/j.jvolgeores.2016.01.002, 2016.

Chim, M. M., Aubry, T. J., Abraham, N. L., Marshall, L., Mulcahy, J., Walton, J., and Schmidt, A.: Climate Projections Very Likely Underestimate Future Volcanic Forcing and Its Climatic Effects, Geophysical Research Letters, 50, e2023GL103 743, https://doi.org/10.1029/2023GL103743, 2023.

Chim, M. M., Stiller, D., and Ziegler, E.: Analysis and figure code for "Stratospheric aerosol forcing for CMIP7 – Part 3: comparison with CMIP6 and evaluation using complementary datasets", https://zenodo.org/records/21385639?preview=1&token=eyJhbGciOiJIUzUxMiJ9.eyJpZCI6IjhlNjAxODg4LTNhYTgtNDA3MS04NThmLWY0M2Y0YWQ4MWUwZiIsImRhdGEiOnt9LCJyYW5kb20iOiJhZjE3MmIzNzNlNDc2Njc5ZjBmZDc0MmZlY2I5NDZiMiJ9.xrQ-dfoB0EmJtPkJk90xxCQr95QXtgcUtVEE0ipl3TvlA4XxXRZgTH9hR4i4NCHtO-bEx5F9W2yTU6_0od_gFA, 2026.

Damadeo, R. P., Sofieva, V. F., Rozanov, A., and Thomason, L. W.: An empirical characterization of the aerosol Ångström exponent interpolation bias using SAGE III/ISS data, Atmospheric Measurement Techniques, 17, 3669–3678, https://doi.org/10.5194/amt-17-3669-2024, 2024.

Damany-Pearce, L., Johnson, B., Wells, A., Osborne, M., Allan, J., Belcher, C., Jones, A., and Haywood, J.: Australian wildfires cause the largest stratospheric warming since Pinatubo and extends the lifetime of the Antarctic ozone hole, Scientific Reports, 12, 12 665, https://doi.org/10.1038/s41598-022-15794-3, 2022.

Danjon, A.: Relation Entre l'Eclairement de la Lune Eclipsee et l'Activite Solaire, L'Astronomie, 35, 261–265, 1921.

Deluisi, J. J., Dutton, E. G., Coulson, K. L., DeFoor, T. E., and Mendonca, B. G.: On some radiative features of the el chichon volcanic stratospheric dust cloud and a cloud of unknown origin observed at Mauna Loa, Journal of Geophysical Research: Oceans, 88, 6769–6772, https://doi.org/10.1029/JC088iC11p06769, 1983.

Dogar, M. M., Sato, T., and Liu, F.: Ocean Sensitivity to Periodic and Constant Volcanism, Scientific Reports, 10, https://doi.org/10.1038/s41598-019-57027-0, 2020.

Dunne, J. P., Hewitt, H. T., Arblaster, J., Bonou, F., Boucher, O., Cavazos, T., Durack, P. J., Hassler, B., Juckes, M., Miyakawa, T., Mizielinski, M., Naik, V., Nicholls, Z., O'Rourke, E., Pincus, R., Sanderson, B. M., Simpson, I. R., and Taylor, K. E.: An evolving Coupled Model

https://doi.org/10.5194/egusphere-2026-4193
Preprint. Discussion started: 23 July 2026

Intercomparison Project phase 7 (CMIP7) and Fast Track in support of future climate assessment, https://doi.org/10.5194/egusphere-2024-3874, 2024.

ETH Zürich: input4MIPs.IACETH.aerosolProperties.CMIP.IACETH-SAGE3lambda-3-0-0, https://doi.org/10.22033/ESGF/INPUT4MIPS.1681, 2017.

Eyring, V., Bony, S., Meehl, G. A., Senior, C. A., Stevens, B., Stouffer, R. J., and Taylor, K. E.: Overview of the Coupled Model Intercomparison Project Phase 6 (CMIP6) experimental design and organization, Geoscientific Model Development, 9, 1937–1958, https://doi.org/10.5194/gmd-9-1937-2016, 2016.

Fang, S., Sigl, M., Toohey, M., Jungclaus, J., Zanchettin, D., and Timmreck, C.: The Role of Small to Moderate Volcanic Eruptions in the Early 19th Century Climate, Geophysical Research Letters, 50, e2023GL105 307, https://doi.org/10.1029/2023GL105307, 2023.

Gao, C., Robock, A., and Ammann, C.: Volcanic forcing of climate over the past 1500 years: An improved ice core-based index for climate models, Journal of Geophysical Research: Atmospheres, 113, 2008JD010 239, https://doi.org/10.1029/2008JD010239, 2008.

García-Gil, A., Muñoz-Tuñón, C., and Varela, A. M.: Atmosphere Extinction at the ORM on La Palma: A 20 yr Statistical Database Gathered at the Carlsberg Meridian Telescope, Publications of the Astronomical Society of the Pacific, 122, 1109–1121, https://doi.org/10.1086/656329, 2010.

Global Volcanism Program: Volcanoes of the World, v.5, https://doi.org/https://doi.org/10.5479/si.GVP.VOTW5-2024.5.2, 2025.

Guillet, S., Corona, C., Oppenheimer, C., Lavigne, F., Khodri, M., Ludlow, F., Sigl, M., Toohey, M., Atkins, P. S., Yang, Z., Muranaka, T., Horikawa, N., and Stoffel, M.: Lunar eclipses illuminate timing and climate impact of medieval volcanism, Nature, 616, 91–95, https://doi.org/10.1038/s41586-023-05751-z, 2023.

Hardie, R. H.: Photoelectric Reductions in Astronomical Techniques, University of Chicago, Chicago, 1962.

Hofmann, D., Barnes, J., Dutton, E., Deshler, T., Jäger, H., Keen, R., and Osborn, M.: Surface-based observations of volcanic emissions to the stratosphere, in: Geophysical monograph series, edited by Robock, A. and Oppenheimer, C., vol. 139, pp. 57–73, American Geophysical Union, Washington, D. C., ISBN 978-0-87590-998-1, https://doi.org/10.1029/139GM04, 2003.

Iacono, M. J., Delamere, J. S., Mlawer, E. J., Shephard, M. W., Clough, S. A., and Collins, W. D.: Radiative forcing by long-lived greenhouse gases: Calculations with the AER radiative transfer models, Journal of Geophysical Research: Atmospheres, 113, 2008JD009 944, https://doi.org/10.1029/2008JD009944, 2008.

Jungclaus, J. H., Bard, E., Baroni, M., Braconnot, P., Cao, J., Chini, L. P., Egorova, T., Evans, M., González-Rouco, J. F., Goosse, H., Hurtt, G. C., Joos, F., Kaplan, J. O., Khodri, M., Klein Goldewijk, K., Krivova, N., LeGrande, A. N., Lorenz, S. J., Luterbacher, J., Man, W., Maycock, A. C., Meinshausen, M., Moberg, A., Muscheler, R., Nehrbass-Ahles, C., Otto-Bliesner, B. I., Phipps, S. J., Pongratz, J., Rozanov, E., Schmidt, G. A., Schmidt, H., Schmutz, W., Schurer, A., Shapiro, A. I., Sigl, M., Smerdon, J. E., Solanki, S. K., Timmreck, C., Toohey, M., Usoskin, I. G., Wagner, S., Wu, C.-J., Yeo, K. L., Zanchettin, D., Zhang, Q., and Zorita, E.: The PMIP4 contribution to CMIP6 – Part 3: The last millennium, scientific objective, and experimental design for the PMIP4 *past1000* simulations, Geoscientific Model Development, 10, 4005–4033, https://doi.org/10.5194/gmd-10-4005-2017, 2017.

Jäger, H. and Deshler, T.: Lidar backscatter to extinction, mass and area conversions for stratospheric aerosols based on midlatitude balloon-borne size distribution measurements, Geophysical Research Letters, 29, 1–4, https://doi.org/10.1029/2002GL015609, 2002.

Jörimann, A., Sukhodolov, T., Luo, B., Chiodo, G., Mann, G., and Peter, T.: REtrieval Method for optical and physical Aerosol Properties in the stratosphere (REMAPv1), Geoscientific Model Development, 18, 6023–6041, https://doi.org/10.5194/gmd-18-6023-2025, 2025.

Keen, R. A.: Volcanic Aerosols and Lunar Eclipses, Science, 222, 1011–1013, https://doi.org/10.1126/science.222.4627.1011, 1983.

Khaykin, S., Podglajen, A., Ploeger, F., Grooß, J.-U., Tence, F., Bekki, S., Khlopenkov, K., Bedka, K., Rieger, L., Baron, A., Godin-Beekmann, S., Legras, B., Sellitto, P., Sakai, T., Barnes, J., Uchino, O., Morino, I., Nagai, T., Wing, R., Baumgarten, G., Gerding, M., Duflot, V., Payen, G., Jumelet, J., Querel, R., Liley, B., Bourassa, A., Clouser, B., Feofilov, A., Hauchecorne, A., and Ravetta, F.: Global perturbation of stratospheric water and aerosol burden by Hunga eruption, Communications Earth & Environment, 3, 316, https://doi.org/10.1038/s43247-022-00652-x, 2022.

Kovilakam, M., Thomason, L. W., Ernest, N., Rieger, L., Bourassa, A., and Millán, L.: The Global Space-based Stratospheric Aerosol Climatology (version 2.0): 1979–2018, Earth System Science Data, 12, 2607–2634, https://doi.org/10.5194/essd-12-2607-2020, 2020.

Kovilakam, M., Thomason, L. W., Verkerk, M., Aubry, T., and Knepp, T. N.: OMPS-LP aerosol extinction coefficients and their applicability in GloSSAC, Atmospheric Chemistry and Physics, 25, 535–553, https://doi.org/10.5194/acp-25-535-2025, 2025.

Leach, N. J., Jenkins, S., Nicholls, Z., Smith, C. J., Lynch, J., Cain, M., Walsh, T., Wu, B., Tsutsui, J., and Allen, M. R.: FaIRv2.0.0: a generalized impulse response model for climate uncertainty and future scenario exploration, Geoscientific Model Development, 14, 3007–3036, https://doi.org/10.5194/gmd-14-3007-2021, 2021.

Luo, B.: Stratospheric aerosol data for use in CMIP6 models – data description., ftp://iacftp.ethz.ch/pub_read/luo/CMIP6/Readme_Data_Description.pdf, 2018.

Lücke, L. J., Schurer, A. P., Toohey, M., Marshall, L. R., and Hegerl, G. C.: The effect of uncertainties in natural forcing records on simulated temperature during the last millennium, Climate of the Past, 19, 959–978, https://doi.org/10.5194/cp-19-959-2023, publisher: Copernicus GmbH, 2023.

Matsushima, S., Zink, J. R., and Hansen, J. E.: Atmospheric extinction by dust particles as determined from three-color photometry of the lunar eclipse of 19 December 1964, The Astronomical Journal, 71, 103, https://doi.org/10.1086/109863, 1966.

McCormick, M. P., Thomason, L. W., and Trepte, C. R.: Atmospheric effects of the Mt Pinatubo eruption, Nature, 373, 399–404, https://doi.org/10.1038/373399a0, number: 6513, 1995.

Murphy, D. M., Abou-Ghanem, M., Cziczo, D. J., Froyd, K. D., Jacquot, J., Lawler, M. J., Maloney, C., Plane, J. M. C., Ross, M. N., Schill, G. P., and Shen, X.: Metals from spacecraft reentry in stratospheric aerosol particles, Proceedings of the National Academy of Sciences, 120, e2313374 120, https://doi.org/10.1073/pnas.2313374120, 2023.

Neely III, R. R. and Schmidt, A.: VolcanEESM: Global volcanic sulphur dioxide (SO2) emissions database from 1850 to present - Version 1.0, https://doi.org/10.5285/76EBDC0B-0EED-4F70-B89E-55E606BCD568, 2016.

O'Neill, B. C., Tebaldi, C., Van Vuuren, D. P., Eyring, V., Friedlingstein, P., Hurtt, G., Knutti, R., Kriegler, E., Lamarque, J.-F., Lowe, J., Meehl, G. A., Moss, R., Riahi, K., and Sanderson, B. M.: The Scenario Model Intercomparison Project (ScenarioMIP) for CMIP6, Geoscientific Model Development, 9, 3461–3482, https://doi.org/10.5194/gmd-9-3461-2016, 2016.

Pauling, A. G., Bushuk, M., and Bitz, C. M.: Robust Inter-Hemispheric Asymmetry in the Response to Symmetric Volcanic Forcing in Model Large Ensembles, Geophysical Research Letters, 48, https://doi.org/10.1029/2021gl092558, 2021.

Peterson, D. A., Berman, M. T., Fromm, M. D., Servranckx, R., Julstrom, W. J., Hyer, E. J., Campbell, J. R., McHardy, T. M., and Lambert, A.: Worldwide inventory reveals the frequency and variability of pyrocumulonimbus and stratospheric smoke plumes during 2013–2023, npj Climate and Atmospheric Science, 8, 325, https://doi.org/10.1038/s41612-025-01188-5, 2025.

Pohl, C., Wrana, F., Rozanov, A., Deshler, T., Malinina, E., Von Savigny, C., Rieger, L. A., Bourassa, A. E., and Burrows, J. P.: Stratospheric aerosol characteristics from SCIAMACHY limb observations: two-parameter retrieval, Atmospheric Measurement Techniques, 17, 4153–4181, https://doi.org/10.5194/amt-17-4153-2024, 2024.

https://doi.org/10.5194/egusphere-2026-4193
Preprint. Discussion started: 23 July 2026

Pohl, C., Niemeier, U., Rozanov, A., Wrana, F., and Von Savigny, C.: Evaluating SCIAMACHY-retrieved and ECHAM-simulated stratospheric aerosol characteristics by their comparison after volcanic eruptions, https://doi.org/10.5194/egusphere-2026-578, 2026.

Remai, C., Zawada, D., Bourassa, A., Dubé, K., Baron, A., Smith, K., Rieger, L., and Degenstein, D.: Stratospheric Aerosol Particle Size Explains Divergent Limb and Solar Occultation Measurements After the Hunga Eruption, Geophysical Research Letters, 53, e2025GL120 243, https://doi.org/10.1029/2025GL120243, 2026.

Rodgers, A. and Toohey, M.: Estimation of SAOD from measurements of Stellar Attenuation 1955-2020, https://doi.org/10.5281/zenodo.18488959, 2026.

Rodgers, B.: The Estimation of Stratospheric Aerosol Optical Depth from Measurements of Stellar Extinction, Master's thesis, University of Saskatchewan, Saskatoon, https://doi.org/10.13140/RG.2.2.32409.90720, 2022.

Rozanov, A.: Satellite data download, https://www.iup.uni-bremen.de/DataRequest/, 2026.

Rozanov, A., Pohl, C., Arosio, C., Bourassa, A., Bramstedt, K., Malinina, E., Rieger, L., and Burrows, J. P.: Retrieval of stratospheric aerosol extinction coefficients from sun-normalized Ozone Mapper and Profiler Suite Limb Profiler (OMPS-LP) measurements, Atmospheric Measurement Techniques, 17, 6677–6695, https://doi.org/10.5194/amt-17-6677-2024, 2024.

Russell, P. B., Swissler, T. J., and McCormick, M. P.: Methodology for error analysis and simulation of lidar aerosol measurements, Applied Optics, 18, 3783, https://doi.org/10.1364/AO.18.003783, 1979.

Sato, M., Hansen, J. E., McCormick, M. P., and Pollack, J. B.: Stratospheric aerosol optical depths, 1850–1990, Journal of Geophysical Research: Atmospheres, 98, 22 987–22 994, https://doi.org/10.1029/93JD02553, 1993.

Schindlbeck-Belo, J. C., Toohey, M., Jegen, M., Kutterolf, S., and Rehfeld, K.: PalVol v1: a proxy-based semi-stochastic ensemble reconstruction of volcanic stratospheric sulfur injection for the last glacial cycle (140 000–50 BP), Earth System Science Data, 16, 1063–1081, https://doi.org/10.5194/essd-16-1063-2024, 2024.

Schmidt, A., Mills, M. J., Ghan, S., Gregory, J. M., Allan, R. P., Andrews, T., Bardeen, C. G., Conley, A., Forster, P. M., Gettelman, A., Portmann, R. W., Solomon, S., and Toon, O. B.: Volcanic Radiative Forcing From 1979 to 2015, Journal of Geophysical Research: Atmospheres, 123, 12 491–12 508, https://doi.org/10.1029/2018JD028776, 2018.

Schneider, J., Weigel, R., Klimach, T., Dragoneas, A., Appel, O., Hünig, A., Molleker, S., Köllner, F., Clemen, H.-C., Eppers, O., Hoppe, P., Hoor, P., Mahnke, C., Krämer, M., Rolf, C., Grooß, J.-U., Zahn, A., Obersteiner, F., Ravegnani, F., Ulanovsky, A., Schlager, H., Scheibe, M., Diskin, G. S., DiGangi, J. P., Nowak, J. B., Zöger, M., and Borrmann, S.: Aircraft-based observation of meteoric material in lower-stratospheric aerosol particles between 15 and 68° N, Atmospheric Chemistry and Physics, 21, 989–1013, https://doi.org/10.5194/acp-21-989-2021, 2021.

Sheng, J., Weisenstein, D. K., Luo, B., Rozanov, E., Stenke, A., Anet, J., Bingemer, H., and Peter, T.: Global atmospheric sulfur budget under volcanically quiescent conditions: Aerosol-chemistry-climate model predictions and validation, Journal of Geophysical Research: Atmospheres, 120, 256–276, https://doi.org/10.1002/2014JD021985, 2015.

Sigl, M., Winstrup, M., McConnell, J. R., Welten, K. C., Plunkett, G., Ludlow, F., Büntgen, U., Caffee, M., Chellman, N., Dahl-Jensen, D., Fischer, H., Kipfstuhl, S., Kostick, C., Maselli, O. J., Mekhaldi, F., Mulvaney, R., Muscheler, R., Pasteris, D. R., Pilcher, J. R., Salzer, M., Schüpbach, S., Steffensen, J. P., Vinther, B. M., and Woodruff, T. E.: Timing and climate forcing of volcanic eruptions for the past 2,500 years, Nature, 523, 543–549, https://doi.org/10.1038/nature14565, 2015.

Sofieva, V., Rozanov, A., and Szelag, M.: Merged aerosol extinction profiles and stratospheric optical depth dataset created using data from several satellite limb and occultation instrumentsClimate data Record of Stratospheric aerosols (CREST), https://doi.org/10.57707/FMI-B2SHARE.DFE14351FD8548BCACA3C2956B17F665, 2024a.

https://doi.org/10.5194/egusphere-2026-4193
Preprint. Discussion started: 23 July 2026

Sofieva, V. F., Rozanov, A., Szelag, M., Burrows, J. P., Retscher, C., Damadeo, R., Degenstein, D., Rieger, L. A., and Bourassa, A.: CREST: a Climate Data Record of Stratospheric Aerosols, Earth System Science Data, 16, 5227–5241, https://doi.org/10.5194/essd-16-5227-2024, 2024b.

SPARC: SPARC Assessment of Stratospheric Aerosol Properties (ASAP), Tech. Rep. SPARC Report No. 4, WMO/ICSU/IOC World Climate Research Programme, https://aparc-climate.org/publications/sparc-report-no-4/, 2006.

Stock, J.: The atmospheric extinction in photoelectric photometry, Vistas in Astronomy, 11, 127–146, https://doi.org/10.1016/0083-6656(69)90008-7, 1969.

Stothers, R.: Stratospheric Transparency Derived from Total Lunar Eclipse Colors, 1665–1800, Publications of the Astronomical Society of the Pacific, 116, 886–893, https://doi.org/10.1086/425537, 2004.

Stothers, R.: Stratospheric Transparency Derived from Total Lunar Eclipse Colors, 1801–1881, Publications of the Astronomical Society of the Pacific, 117, 1445–1450, https://doi.org/10.1086/497016, 2005.

Stothers, R. B.: Major optical depth perturbations to the stratosphere from volcanic eruptions: Pyrheliometric period, 1881–1960, Journal of Geophysical Research: Atmospheres, 101, 3901–3920, https://doi.org/10.1029/95JD03237, 1996.

Stothers, R. B.: Major optical depth perturbations to the stratosphere from volcanic eruptions: Stellar extinction period, 1961–1978, Journal of Geophysical Research: Atmospheres, 106, 2993–3003, https://doi.org/10.1029/2000JD900652, 2001.

Stothers, R. B.: Three centuries of observation of stratospheric transparency, Climatic Change, 83, 515–521, https://doi.org/10.1007/s10584-007-9238-3, 2007.

Stothers, R. B.: A Comparison of Stellar Extinction and Space-Based Measurements of Stratospheric Aerosol Optical Depth, Publications of the Astronomical Society of the Pacific, 121, 303–306, https://doi.org/10.1086/598224, 2009.

Taha, G., Loughman, R., Zhu, T., Thomason, L., Kar, J., Rieger, L., and Bourassa, A.: OMPS LP Version 2.0 multi-wavelength aerosol extinction coefficient retrieval algorithm, Atmospheric Measurement Techniques, 14, 1015–1036, https://doi.org/10.5194/amt-14-1015-2021, 2021.

Theys, N., De Smedt, I., Van Roozendael, M., Froidevaux, L., Clarisse, L., and Hendrick, F.: First satellite detection of volcanic OClO after the eruption of Puyehue-Cordón Caulle, Geophysical Research Letters, 41, 667–672, https://doi.org/10.1002/2013GL058416, 2014.

Thomason, L. W., Ernest, N., Millán, L., Rieger, L., Bourassa, A., Vernier, J.-P., Manney, G., Luo, B., Arfeuille, F., and Peter, T.: A global space-based stratospheric aerosol climatology: 1979–2016, Earth System Science Data, 10, 469–492, https://doi.org/10.5194/essd-10-469-2018, 2018.

Toohey, M. and Sigl, M.: Volcanic stratospheric sulfur injections and aerosol optical depth from 500 BCE to 1900 CE, Earth System Science Data, 9, 809–831, https://doi.org/10.5194/essd-9-809-2017, 2017.

Verkerk, M., Aubry, T. J., Smith, C., Hopcroft, P. O., Sigl, M., Tierney, J. E., Anchukaitis, K., Osman, M., Schmidt, A., and Toohey, M.: Using reduced-complexity volcanic aerosol and climate models to produce large ensemble simulations of Holocene temperature, Climate of the Past, 21, 1755–1778, https://doi.org/10.5194/cp-21-1755-2025, publisher: Copernicus GmbH, 2025.

Wiart, P. and Oppenheimer, C.: Largest known historical eruption in Africa: Dubbi volcano, Eritrea, 1861, Geology, 28, 291, https://doi.org/10.1130/0091-7613(2000)28<291:LKHEIA>2.0.CO;2, 2000.

Xing, C., Liu, F., Wang, B., Chen, D., Liu, J., and Liu, B.: Boreal Winter Surface Air Temperature Responses to Large Tropical Volcanic Eruptions in CMIP5 Models, Journal of Climate, 33, 2407–2426, https://doi.org/10.1175/JCLI-D-19-0186.1, 2020.

https://doi.org/10.5194/egusphere-2026-4193
Preprint. Discussion started: 23 July 2026

Yu, P., Murphy, D. M., Portmann, R. W., Toon, O. B., Froyd, K. D., Rollins, A. W., Gao, R., and Rosenlof, K. H.: Radiative forcing from anthropogenic sulfur and organic emissions reaching the stratosphere, Geophysical Research Letters, 43, 9361–9367, https://doi.org/10.1002/2016GL070153, 2016.

Zanchettin, D., Khodri, M., Timmreck, C., Toohey, M., Schmidt, A., Gerber, E. P., Hegerl, G., Robock, A., Pausata, F. S. R., Ball, W. T., Bauer, S. E., Bekki, S., Dhomse, S. S., LeGrande, A. N., Mann, G. W., Marshall, L., Mills, M., Marchand, M., Niemeier, U., Poulain, V., Rozanov, E., Rubino, A., Stenke, A., Tsigaridis, K., and Tummon, F.: The Model Intercomparison Project on the climatic response to Volcanic forcing (VolMIP): experimental design and forcing input data for CMIP6, Geoscientific Model Development, 9, 2701–2719, https://doi.org/10.5194/gmd-9-2701-2016, 2016.

Zawada, D. J., Rieger, L. A., Bourassa, A. E., and Degenstein, D. A.: Tomographic retrievals of ozone with the OMPS Limb Profiler: algorithm description and preliminary results, Atmospheric Measurement Techniques, 11, 2375–2393, https://doi.org/10.5194/amt-11-2375-2018, 2018.

Ångström, A.: On the Atmospheric Transmission of Sun Radiation and on Dust in the Air, Geografiska Annaler, 11, 156–166, https://doi.org/10.1080/20014422.1929.11880498, 1929.